Détection de fuites d'eau par drone à l'aide de l'imagerie thermique et de l'analyse du réseau de drainage

par

Basile LALLEMENT

MÉMOIRE PAR ARTICLE PRÉSENTÉ À L'ÉCOLE DE TECHNOLOGIE SUPÉRIEURE COMME EXIGENCE PARTIELLE À L'OBTENTION DE LA MAÎTRISE AVEC MÉMOIRE EN GÉNIE DE L'ENVIRONNEMENT
M. Sc. A

MONTRÉAL, LE 26 MARS 2025

ÉCOLE DE TECHNOLOGIE SUPÉRIEURE
UNIVERSITÉ DU QUÉBEC

PRÉSENTATION DU JURY

CE MÉMOIRE A ÉTÉ ÉVALUÉ

PAR UN JURY COMPOSÉ DE :

M. Michel Baraër, directeur de mémoire
Département de génie de la construction à l'École de technologie supérieure

M. Eric Rosa, codirecteur de mémoire
Institut de recherche en mines et en environnement
Université du Québec en Abitibi-Témiscamingue

Mme Annie Poulin, présidente du jury
Département de génie de la construction à l'École de technologie supérieure

M. Jonathan Aubertin, membre du jury
Département de génie de la construction à l'École de technologie supérieure

IL A FAIT L'OBJET D'UNE SOUTENANCE DEVANT JURY ET PUBLIC

LE 21 MARS 2025

À L'ÉCOLE DE TECHNOLOGIE SUPÉRIEURE

REMERCIEMENTS

Je tiens particulièrement à remercier mon directeur de recherche, M. Michel Baraer, pour m'avoir fait confiance dès les premiers instants du projet, et pour m'avoir soutenu et accompagné tout au long de mon mémoire. Son expertise et son encadrement m'ont été d'une aide précieuse et m'ont permis de développer des compétences en hydrologie et en télédétection qui m'ont été indispensables pour la réalisation de ce travail.

Je souhaite également remercier mes co-directeurs de recherche, M. Vincent Cloutier, et M. Éric Rosa, ainsi que M. Brahim Maylal, pour leur accueil chaleureux, et le partage de leurs connaissances essentielles au bon déroulement du projet, sans qui je n'aurai jamais pu mener à bien mes recherches.

Je remercie également tous mes collègues du laboratoire HC3, pour les moments partagés ensemble, pour leur aide et leur motivation qui ont été des atouts inestimables. Je remercie tout particulièrement mon collègue Omar, avec qui j'ai partagé ce projet ambitieux et dont je salue l'important travail qu'il a pu accomplir.

Enfin, je tenais à remercier ma famille et mon ami Jeremy pour leurs encouragements et leur soutien constant.

Détection de fuites d'eau par drone à l'aide de l'imagerie thermique et de l'analyse du réseau de drainage

Basile LALLEMENT

RÉSUMÉ

Limiter les risques de contamination des milieux naturels et ses conséquences pour la santé publique constituent deux priorités dans la gestion des risques environnementaux dans le secteur minier. Les bassins à résidus, souvent à ciel ouvert, concentrent une grande quantité de métaux toxiques représentant une source potentielle de contamination. Du fait de leur haute mobilité à la suite d'événements tels que des précipitations, des infiltrations d'eau ou encore des cycles de gel et dégel, ces sites font l'objet d'une surveillance particulière. Cette surveillance consiste notamment en la détection d'éventuelles fuites ou zones humides qui entraineraient la dispersion de métaux traces et provoqueraient la dégradation des écosystèmes environnants. Dans ce contexte, les progrès technologiques en matière de drones et de capteurs d'imagerie offrent de nouvelles opportunités.

L'étude présentée s'est déroulée sur le site minier Quémont 2, de la Fonderie Horne, située à Rouyn Noranda, au Québec. Certains ouvrages de retenu du site vieillissant, des pertes d'eau peuvent apparaître à leur base. Localiser les fuites est souvent très difficile à réaliser sans moyen technologique compte tenu de la surface du site, et la présence de végétation, de zones d'ombre et de roches de tailles diverses. Pour y remédier, la méthode présentée ici propose d'exploiter simultanément des images thermiques et visibles capturées à partir de drone. L'imagerie infrarouge (IR) permet de repérer des contrastes de température, indicateurs probables de la présence d'eau, tandis que les images haute définition du visible servent à générer des images matricielles secondaires (vNDVI, ombrages, pentes) utilisés pour filtrer les faux positifs inclus dans les images thermiques. Le vNDVI (visible NDVI), par exemple, permet d'isoler des surfaces végétalisées susceptibles de présenter une signature thermique proche de celle de l'eau. Les pentes et ombrage aident quant à eux à identifier les artefacts dus à la topographie ou à l'ombre. Un seuillage des données par l'utilisation d'algorithmes d'apprentissage automatique est également mis à profit, améliorant la précision des traitements et l'autonomie de l'approche, tout en réduisant le temps d'analyse. Finalement, ce prétraitement par imagerie permet le traçage d'un réseau de drainage afin de distinguer les possibles ruissellements d'eau souterraines de ceux de surface. Les résultats obtenus montrent que cette approche intégrée isole efficacement les résurgences et met en évidence les suintements observés rendant possible l'identification les sources potentielles d'exfiltrations, facilitant la planification des opérations humaines et la prise de décision. La méthode proposée est adaptable à diverses questions de surveillance environnementale. Ses limites actuelles sont liées principalement à la performance du capteur thermique et aux conditions météorologiques à la prise d'image.

Mots-clés: Détection d'exfiltrations, Hydrologie, Surveillance environnementale, vNDVI, IR

Drone-based water leak detection using thermal imaging and drainage network analysis

Basile LALLEMENT

ABSTRACT

Environmental risk management in the mining sector is a major issue to limit the risks of contamination of natural environments and the consequences on human health. Tailings ponds, often open-air, concentrate a large quantity of toxic metals representing a potential source of contamination. Due to their high mobility following events such as precipitation, water infiltration, or freeze-thaw cycles, increased monitoring of these mining sites is therefore essential. This monitoring involves the detection and prevention of possible leaks or wetlands that would cause the dispersion of trace metals and lead to the degradation of surrounding ecosystems. In this context, technological advances in drones and imaging sensors offer new opportunities.

The study presented was conducted at the Quémont 2 mining site of the Horne smelter, located in Rouyn-Noranda, Quebec. Some of the site's aging retention structures may experience water losses at their base. Locating leaks is often very difficult without technological means due to the site's large surface area and the presence of vegetation, shaded areas, and rocks of various sizes. To address this, the method presented proposes to simultaneously exploit thermal and visible images captured by a drone. Infrared (IR) imaging makes it possible to detect temperature contrasts, probable indicators of the presence of water, while high-definition visible images are used to generate secondary rasters (vNDVI, shading, slopes) that help filter false positives included in thermal images. For example, vNDVI (visible NDVI) allows the isolation of vegetated surfaces that may have a thermal signature similar to that of water. Slopes and shading help identify artifacts caused by topography or shadows. Data thresholding using machine learning algorithms is also employed, improving processing accuracy and the autonomy of the approach while reducing analysis time. Finally, this imaging preprocessing enables the tracing of a drainage network to distinguish possible groundwater runoff from surface runoff. The results obtained show that this integrated approach effectively isolates resurgences and highlights observed seepages, making it possible to identify potential sources of exfiltrations, thereby facilitating the planning of human operations and decision-making. The proposed method is adaptable to various environmental monitoring applications. Its current limitations are mainly related to the performance of the thermal sensor and the meteorological conditions at the time of image acquisition.

Keywords: Water Seepage, Remote Sensing, Hydrology, Environmental Monitoring, Image Processing, vNDVI, UAV, IR

TABLE DES MATIÈRES

Page

LISTE DES FIGURES

LISTE DES ABRÉVIATIONS, SIGLES ET ACRONYMES

AI	Intelligence artificielle
CMOS	Complementary metal oxide semiconductor
DTM	Digital terrain model
ERT	Tomographie de résistivité électrique
GPR	Ground-penetrating radar
IR	Infrarouge
IRT	Infrared thermography
PS	Polarisation spontanée
RGB	Red green blue
MASW	Analyse multiple des ondes de surfaces
MNT	Modèle numérique de terrain
NDVI	Normalized difference vegetation index
NIR	Proche Infrarouge
SIG	Système d'information géographique
UAV	Unmanned aerial vehicle
vNDVI	Visible normalized difference vegetation index

LISTE DES SYMBOLES ET UNITÉS DE MESURE

αS	Azimut solaire	°
γS	Élévation angulaire solaire	°
RH	Humidité relative	%
T	Température	°C
WS	Vitesse du vent	km/h
V	Volume d'eau	m^3

INTRODUCTION

Les environnements miniers, en particulier les sites à résidus miniers, suscitent un intérêt grandissant en matière de surveillance environnementale et de gestion des risques. En effet, la phase d'entreposage des résidus représente une source potentielle de contamination des écosystèmes, notamment lorsque des exfiltrations d'eau ou des suintements se produisent à travers les digues de confinement (Song et al., 2020 ; Kossoff et al., 2014). Dans un tel contexte, la détérioration progressive des structures de retenue, voire la fragilisation des digues, peut conduire à la dispersion de métaux traces ou de sulfates, lesquels constituent un enjeu majeur de santé publique et de préservation de l'environnement (Ghomshei & Allen, 2000 ; Chen et al., 2021). Il est donc crucial de développer des méthodes de surveillance à la fois efficaces, non invasives et adaptées à la variabilité spatio-temporelle des sites miniers.

Grâce aux avancées technologiques récentes, la télédétection par drone (UAV) et la miniaturisation des capteurs embarqués, offrent désormais de nouvelles opportunités pour la caractérisation et le suivi de l'état de ces sites miniers (Manfreda et al., 2018 ; Whitehead & Hugenholtz, 2014). Les drones peuvent être équipés d'une multitude de capteurs : caméras visibles haute résolution, capteurs multispectraux et caméras thermiques infrarouges, permettant d'acquérir des images à résolution sur de vastes superficies et avec une grande répétabilité. Dans des applications antérieures, l'imagerie thermique a prouvé son intérêt pour détecter des variations de température à la surface d'ouvrages comme des digues en béton ou en terre (Garrido et al., 2020 ; Li et al., 2024). Toutefois, les digues de résidus miniers, parfois vieilles de plusieurs décennies, se révèlent plus complexes à analyser : la présence de végétation, de surfaces rocheuses fracturées, ou de micro-reliefs engendre des contrastes thermiques pouvant générer des « faux positifs » (Pandey et al., 2013 ; Mundy et al., 2017).

Pour surmonter ces obstacles, le choix d'une approche combinée de plusieurs méthodes menant à plusieurs indices apparaît particulièrement pertinent (Hung et al., 2019 ; Costa et al., 2020). En complément de l'imagerie thermique, la caméra visible haute résolution peut permettre de produire une orthomosaïque RGB à partir de laquelle on peut dériver plusieurs images matricielles secondaires, comme l'indice de végétation « vNDVI » (visible NDVI) calculé uniquement à partir des bandes rouge (R), verte (G) et bleu (B), et qui se révèle efficace pour repérer la végétation (Costa et al., 2020). Contrairement à l'indice NDVI qui est calculé à partir d'une caméra multispectrale, le vNDVI n'a donc besoin que des trois bandes du visible pour être calculé, et dont la marge d'erreur est seulement d'environ 6,89% en comparaison avec le NDVI. Le NDVI est largement utilisé en environnement ou en agriculture pour le suivi des cultures ou des forêts (Baluja et al., 2012; Zhang, Wu, Zhang, Jiao, & Li, 2012; Anderson et al., 2008), et dont le vNDVI rend cet indice encore plus accessible. D'autres images matricielles sont également calculées à partir du modèle numérique de terrain (MNT), particulièrement adapté pour isoler l'influence de la topographie ou des zones d'ombre risquant de mimer le signal de l'eau, par l'obtention des images matricielles représentant les pentes et l'ombrage (Barbieri et al., 2011).

L'imagerie par drone peut être également intégrée à divers processus d'analyse d'images, avec ou sans recours à l'intelligence artificielle (IA), pour la segmentation d'images, l'analyse de texture ou la détection d'objets (Blaschke et al., 2000; Bharati, Liu, & MacGregor, 2004; Hung, Song, & Lan, 2019; Xu, Xu, Jin, & Song, 2011). Pour la détection de fuites ou de suintements, la thermographie infrarouge (TIR) s'impose progressivement comme l'une des meilleures techniques de contrôle non destructif (Garrido, Lagüela, Otero, & Arias, 2020 ; Deitchman & Loheide II, 2009). Cela est particulièrement vrai dans des contextes où les surfaces de fond sont relativement homogènes, comme les barrages en béton ou les digues (Li et al., 2024 ; Thomson et al., 2015). Dans ces contextes, l'utilisation d'algorithmes d'IA complexes permet d'identifier automatiquement les suintements en surface des barrages à partir de thermogrammes collectés par drone équipé d'une caméra thermique. Comparée à la méthode de reconnaissance à partir du visible, l'imagerie thermique infrarouge permet d'identifier l'emplacement et l'étendue des risques de fuite, notamment la nuit (Wang, Liang, & Rongliang, 2024).

Les études menées sur des structures de retenue réelles soulignent la polyvalence et les capacités d'acquisition de données haute résolution des drones commerciaux modernes équipés de caméras IRT (Llerena & Sattarvand, 2023). En revanche, les environnements plus complexes, tels que les digues de résidus miniers vieilles de plusieurs décennies, nécessitent encore des améliorations méthodologiques et/ou technologiques pour détecter efficacement les fuites mineures ou les suintements. La végétation, la complexité des arrière-plans, un faible rapport signal/bruit et une résolution thermique limitée affectent significativement les résultats automatisés (Wang et al., 2022). Dans ces environnements, l'interprétation des images thermiques reste limitée par divers facteurs, notamment des problèmes techniques liés à l'acquisition des images, les variations diurnes du rayonnement et de la température, ainsi que l'hétérogénéité des parois rocheuses (Pandey, Gleeson, & Baraer, 2013; Mundy, Gleeson, Roberts, Baraer, & McKenzie, 2017).

Dans ces contextes, le traitement d'image en profondeur et l'apprentissage automatique montrent actuellement leurs limites pour identifier avec précision les dangers cachés (Wang et al., 2024). Les efforts de recherche récents s'attaquent à ces défis en cherchant à améliorer les algorithmes d'apprentissage automatique appliqués aux modèles thermiques basés sur la photogrammétrie afin d'identifier les fuites dans les structures de retenue (Gomez Llerena, Ghahramanieisalou, & Sattarvand, 2023 ; Llerena & Sattarvand, 2023). Une autre approche consiste à augmenter le nombre de composants utilisés pour l'application de l'IA en télédétection dans la surveillance environnementale (Janga, Asamani, Sun, & Cristea, 2023 ; Khonina et al., 2024). Le défi réside dans la génération de multiples trames d'intérêt à partir d'une seule source de données tout en minimisant le temps d'acquisition des données.

Au-delà de la simple détection de zones humides ou de suintements, l'autre enjeu est de contextualiser ces fuites dans le réseau hydrologique. L'apparition d'exfiltrations ponctuelles au sein d'un bassin minier peut provenir de circulations souterraines complexes, notamment dans un socle rocheux fracturé ou via un substrat argileux poreux (El Mrabet, 2021). Aussi, modéliser ou simuler les lignes de drainage, à partir d'un MNT, permet de reconstituer les trajectoires d'écoulement et de différencier les ruissellements de surface des résurgences souterraines (Manfreda et al., 2018). En superposant la carte rassemblant l'ensemble des zones identifiées à un réseau de drainage simulé, il est possible d'identifier les sources probables de ces écoulements et de relier plusieurs zones humides successives (Morgan & Colins, 2022).

La présente étude a été réalisée au site Quémont 2, au nord de Rouyn-Noranda (Québec), où le parc à résidus miniers présente un ensemble de digues plus ou moins anciennes (D, E, F, G), ceinturant des résidus potentiellement riches métaux lourds, et dans un contexte hydrogéologique complexe (El Mrabet, 2021 ; Mhiri, 2023). Des suintements déjà observés sur le terrain incitent à recourir à une méthode non invasive de surveillance et de cartographie. L'approche proposée consiste à effectuer des vols de drones munis d'une double caméra (visible et thermique), puis de traiter les données pour générer des indicateurs primaires (orthomosaïques IR/RGB) et secondaires (vNDVI, pente, ombrage), suivis par un seuillage des valeurs, d'une analyse texturale et, enfin, d'une analyse hydrologique. L'objectif est de mettre en évidence la localisation précise des zones humides et des écoulements d'eau à la base des digues et de différencier les sources primaires de leur évacuation par le réseau de drainage du site.

CHAPITRE 1

REVUE DE LITTÉRATURE

1.1 Environnements miniers

Cette section 1.1 se concentrera sur la définition et la description des environnements propres aux sites d'extraction et de dépôts de résidus miniers. La section 1.1.1 présentera les caractéristiques et les propriétés des sites miniers, et la section 1.1.2 visera à présenter les risques de pollution et de contamination, ainsi que les enjeux de la surveillance environnementale dans un contexte minier. Enfin, la section 1.1.3 introduira une contextualisation de l'étude par la présentation du site d'étude.

1.1.1 Caractéristiques et propriétés des sites miniers

Les environnements issus d'activités minières présentent des aires ayant des caractéristiques structurelles et physico-chimiques environnementales spécifiques liées à la nature des résidus, à la structure géologique des sous-sols et aux modes d'exploitation (Song, Song, Gu, & Li, 2020). Ils se composent en général de trois zones principales constituées de l'aire d'extraction (à ciel ouvert ou souterraine), des installations de traitement (concassage, flottation, fonderie) et des bassins ou digues entreposant les déchets ou résidus miniers (Kossoff et al., 2014). Ces rejets sont parfois susceptibles de contenir des sulfures (pyrite, chalcopyrite) et divers métaux (Cu, Pb, Zn), qui constituent un enjeu majeur pour l'eau et les sols (El Mrabet, 2021). Les sites miniers présentent bien souvent des stériles fins ou grossiers dont la granulométrie peut fortement influencer la porosité, et donc la perméabilité, la stabilité et la rétention d'eau (Gareev & Gareev, 2023; Sourkova, Frouz, & Santruckova, 2005). Dépendamment de la nature des minerais extraits et de la méthode d'entreposage, la composition géochimique riche en sulfures de ces résidus provoque une oxydation importante et engendre un drainage minier acide favorisant la libération de métaux traces (Shrestha & Lal, 2011). Ces espaces de stockage sont primordiaux pour limiter la dispersion de ces éléments et limiter les impacts environnementaux. Cependant la stabilité géotechnique peut être compromise par l'érosion et les processus hydrologiques, dont l'impact varie fortement selon les matériaux utilisés pour la construction des digues de confinement (Feng, Wang, Bai, & Reading, 2019; Ramani, 2012).

1.1.2 Contamination et enjeux environnementaux

L'entreposage des déchets miniers et des stériles constitue la première étape pour limiter la contamination des milieux naturels environnants. Souvent entreposés entre des digues de rétention ou des haldes, ils sont pourtant sujets à de nombreux vecteurs de dispersion (Hou et al., 2023), constituant un défi humain permanent. Les facteurs climatiques jouent un rôle important dans la mobilité, la diffusion des métaux traces, et la vitesse à laquelle ils contaminent leur environnement.

L'action combinée de la température, du vent et des précipitations modifie la réactivité chimique des résidus, favorisant ou limitant l'oxydation des sulfures (Punia, 2021). Dans des régions au climat aride à sec, les températures élevées contribuent fortement à la formation de sels efflorescents très riches en métaux, qui sont ensuite déplacés par le vent sur de longues distances. Dans les zones humides, l'abondance en eau accélère la formation des drains miniers acides (AMD). Lorsque l'eau s'infiltre à travers des dépôts de résidus sulfatés, elle se charge en métaux et sulfates, provoquant une contamination acide des sols, des ruisseaux et des nappes. Le drainage acide est particulièrement dévastateur car il se propage sur plusieurs kilomètres et transforme la chimie des écosystèmes (Karaca, Cameselle, & Reddy, 2018). De nombreuses études (Hou et al., 2023) démontrent que l'on dépasse régulièrement les seuils tolérables de métaux traces (As, Cd, Pb, Hg) dans les sols et sédiments autour des exploitations aurifères, mettant en évidence la toxicité potentielle pour l'Homme et les êtres vivants. Ce problème produit potentiellement une accumulation biologique. C'est le cas par exemple du mercure, qui une fois présent dans le milieu aquatique, peut s'y transformer en méthylmercure, un neurotoxique qui remonte la chaîne alimentaire et affecte poissons, mammifères et hommes (Wong, Gauthier, & Nriagu, 1999).

Plusieurs voies de contamination se distinguent pour expliquer la dispersion de ces composés toxiques. L’eau de ruissellement et d’infiltration s’avère être un vecteur central. C’est le cas par exemple des résidus soufrés, dont la génération d’eaux à bas pH (drains acides) entraîne la solubilisation et la migration de fortes concentrations de métaux (Rosner & van Schalkwyk, 1999). De plus, les épisodes de précipitations intenses ou de fonte nivale au printemps constituent des phases critiques durant lesquelles les résidus accumulés dans la neige fondent brutalement, libérant des métaux en forte concentration (Gustaytis, Myagkaya, & Chumbaev, 2018). Le vent constitue également un important vecteur. Des émissions de poussières chargées en éléments toxiques se produisent sur des sites de dépôts à ciel ouvert, ou lorsque les sols sont trop secs pour se stabiliser. Ces poussières retombent ensuite en dehors du site, et parfois même à plusieurs dizaines de kilomètres, contaminant champs, zones résidentielles et autres écosystèmes (Romero et al., 2015). L’interaction entre les facteurs climatiques et les caractéristiques intrinsèques des résidus explique pourquoi certains secteurs localisés à proximités de mines se retrouvent fortement pollués. Les cas recensés en Afrique du Sud (Rosner & van Schalkwyk, 1999) ou au Canada (Wong, Gauthier, & Nriagu, 1999) montrent, par exemple, des sols superficiels acidifiés et phytotoxiques, par la présence d’importantes teneurs en métaux toxiques (Co, Ni, Zn, Hg).

La diversité des composés et la quantité grandissante des déchets miniers, combinées aux défis environnementaux engendrés par la toxicité de ces composés, poussent l’industrie minière et les gouvernements à mieux surveiller ces sites, et forcent davantage à innover dans les méthodes de télédétection utilisées.

1.1.3 Description du site d’étude

Le site Quémont 2, propriété de Glencore Fonderie Horne, est un parc à résidus miniers situé au nord-est du centre de Rouyn-Noranda, au Québec, au nord du lac Dufault et au sud du lac Osisko. Vaste d’une superficie estimée à 102 hectares, il est stratégiquement situé à proximité d'un environnement urbain et d’un lacustre fragile. Constitué d'un parc à résidus vieillissant en cours de réhabilitation, et surmonté d'une digue principale (Digue G) séparant l'« ancien parc » du « nouveau parc », il est entouré par plusieurs digues plus anciennes (D, E et F), s'appuyant sur un substrat rocheux fracturé et composé localement d'argile, et délimitant la zone minière du milieu naturel (El Mrabet, 2021). Ce contexte hydrologique et géologique particulier rend difficile la gestion de l'eau, notamment en raison du réseau d'écoulements souterrains, résultats des processus d'infiltrations hydrologiques à travers les cavités rocheuses formant le site, et qui risque la migration diffuse de contaminants vers l'extérieur du site.

Au cours des travaux réalisés sur le site (El Mrabet, 2021), des méthodes géophysiques ont été utilisées pour analyser l'hétérogénéité des résidus et des digues, et en déduire la distribution des infiltrations et des zones de saturation. Parmi les méthodes utilisées, la tomographie de résistivité électrique (ERT) a permis de détecter des contrastes de résistivité en lien avec la teneur en eau, la granulométrie et la fracturation, et également d'estimer certaines propriétés hydrologiques telles que la porosité et la conductivité hydraulique. Dans des recherches antérieures, l'ERT a démontré son efficacité à quantifier les voies d'infiltration préférentielles, qu'il s'agisse de digues de rétention ou de bassins à résidus (Moreira et al., 2022 ; Jian et al., 2024).

Dans le cadre de l'utilisation du géoradar (GPR), celui-ci a été utilisé pour affiner l'analyse la structure interne des résidus. Utilisé seul (Poisson et al., 2009) ou associé à d'autres méthodes géophysiques tels que la polarisation spontanée (PS) ou l'analyse multipiste des ondes de surface (MASW) (Adetokunbo et al., 2024), le GPR a aidé à l'identification des zones de fissuration ainsi qu'à l'estimation de la teneur en eau de la couche supérieure du sol. Sur le site de Quémont 2, cette combinaison d'approches a déjà permis de mieux comprendre l'impact de la structure des digues et des particularités géologiques du site, sur l'écoulement des eaux souterraines.

Un premier bilan hydrique a été calculé suite à différentes mesures menées sur le site Quémont 2, mettant en évidence une estimation des flux de sortie via les réseaux d'infiltration avancés par les méthodes géophysiques utilisés (Mhiri, 2023). Ainsi, une perte d’eau par exfiltration depuis le site de rétention vers l’aquifère pourrait atteindre un débit de 3000 m³/jour. Cette estimation traduit l’importance d’identifier les sources de ces exfiltrations. Malgré les données fournies par la résistivité électrique et le GPR, la détection plus précise des infiltrations localisées nécessite des techniques non invasives supplémentaires.

C’est dans cette optique que l'utilisation de méthodes de télédétection aérienne à l'aide d'un drone équipé, entre autres, d'une caméra thermique infrarouge (IR) et d'une caméra haute résolution, permettrait par exemple d'identifier les variations de température pouvant être attribuées aux exfiltrations d'eau de surface.

1.2 Télédétection et outils d’analyse

La section 1.2 sera consacrée à la présentation des techniques de télédétection en environnement et des outils d’analyse par imagerie et en hydrologie, avec une section 1.2.1 se concentrant sur l’imagerie aérienne générales de télédétection en environnement, suivie de la section 1.1.2 qui se concentrera sur les techniques d’analyse d’images.

1.2.1 Imagerie aérienne

L’augmentation importante du nombre de satellites, ainsi que les progrès technologiques rapides ont permis de doter les satellites de capteurs de mesure de plus en plus précis et d’en faire une source de donnée SIG fiable et performante. Les prises de vue satellites ont progressivement ouvert la voie à l’observation et au suivi de facteurs géophysiques utiles dans de nombreux domaines environnementaux, et l’imagerie satellite s’est vite imposée comme une technique de télédétection largement utilisée (Song, Song, Gu & Li, 2020). Cependant, l’imagerie satellite est rapidement confrontée à des limites importantes en termes de résolution spatiale et temporelle, qui sont souvent insuffisantes pour la compréhension de la microtopographie ou la dynamique rapide de certains phénomènes, ou encore le coût élevé de l’acquisition de scènes à haute résolution lorsque disponibles.

Ces dernières décennies ont été marquées par l'émergence de progrès technologiques considérables et la démocratisation des drones (UAV), grâce à la miniaturisation de leurs composants et à la diversification des capteurs embarqués (Manfreda et al., 2018; Whitehead et Hugenholtz, 2014). Le déploiement de caméras haute résolution (RGB), multispectrales ou thermiques/infrarouges (IR) sur des plateformes légères et maniables, offrent un compromis jusque-là inégalé entre cadence d'acquisition de données aériennes, résolution spatiale et coût d'exploitation (Lega et Napoli, 2010; Still et al., 2019). Que ce soit dans des contextes environnementaux ou agricoles, il est à présent possible d'acquérir des images de très haute résolution, souvent de l'ordre du centimètre, et de répéter des mesures nécessitant une fréquence répétée et à la demande, ce qui était beaucoup plus difficile et onéreux avec l'utilisation de satellites ou par le recours à l'aviation habitée (Manfreda et al., 2018).

Outre l'utilisation des bandes visibles, le recours à l'imagerie thermique (typiquement dans la bande 7,5–13,5 µm) s'est lui aussi fortement développé (Whitehead et Hugenholtz, 2014; Manfreda et al., 2018). Les caméras IR, plus légères, permettent la détection des contrastes de température directement liés à l'humidité du sol, ou à l'état hydrique ou physiologique des plantes, ainsi qu'à la détection d'éventuels suintements sur des digues (Garrido, Laguela, Otero et Arias, 2020) ou de pollutions sur un plan d'eau (Lega et Napoli, 2010). Parmi les exemples d'applications possibles comme l'agriculture, l'imagerie thermique permet d'estimer la température de la canopée pour évaluer le stress hydrique, se basant sur le fait que les cultures irriguées ont souvent une température plus basse du fait de l'évapotranspiration (Song et al., 2020). Plus largement, comme dans des contextes de suivi environnemental, la thermographie infrarouge peut repérer des infiltrations d'eau contaminée ou des zones humides imprévues, détectables par un gradient thermique (Manfreda et al., 2018). De plus, les avancées constantes en traitement d'image et en calibration sur le terrain, combinées à la facilité de déploiement des drones, ont permis des progrès significatifs, rendant l'approche thermique abordable et polyvalente.

Parmi les nombreux indices qu'offrent l'imagerie multispectrale, l'indice de végétation qui est apparu ces dernières décennies, le NDVI (Normalized Difference Vegetation Index), est aujourd'hui l'un des plus employés et étudiés (Rouse et al., 1973; Costa et al., 2020). Il met à profit la différence de réflectance entre le rouge et le proche infrarouge (NIR), fournissant ainsi un indicateur fiable de l'activité photosynthétique et de la biomasse verte. Jusque-là calculé uniquement depuis des capteurs satellitaires ou des caméras multispectrales montées sur des avions, il est désormais possible d'en équiper un drone pour plus de flexibilité et d'adaptabilité. La limite principale de cette pratique reste néanmoins le prix élevé comparé aux capteurs RGB traditionnels (Costa et al., 2020).

C'est pourquoi, afin de tirer parti des drones déjà équipés d'une simple caméra RGB haute résolution, de récentes études ont proposé des approches permettant d'estimer le NDVI ou un indice équivalent à partir du spectre visible. C'est le cas du vNDVI (visible NDVI) proposé par Costa et al. (2020), qui grâce à une estimation par approche génétique algorithmique, parvient à reproduire de manière convaincante la variabilité spatiale des NDVI réels. La cartographie du vNDVI obtenue est donc similaire à celui du NDVI ordinaire, mais calculée uniquement à partir des composantes rouge, verte et bleue d'un capteur standard. L'utilisation d'un tel indice approximé est cependant susceptible d'introduire une incertitude plus élevée qu'avec un capteur NIR, mais constitue une alternative à faible coût pour le suivi rapide de la vigueur de la végétation dans des applications comme la surveillance agronomique ou la détection d'anomalies de croissance.

1.2.2 Outils d'analyse par imagerie

L'acquisition de données issues de diverses méthodes de télédétection ne constituent pas la seule étape nécessaire à l'analyse, et doit être associée à d'autres outils pour pouvoir extraire et filtrer l'information désirée. La segmentation d'images constitue un enjeu crucial dans la plupart des domaines de traitement du signal et de l'analyse visuelle, qu'il s'agisse de télédétection, de surveillance, de cartographie urbaine ou d'applications médicales. L'objectif de cette technique est de diviser automatiquement une image en régions homogènes afin de faciliter l'interprétation ultérieure (Barbieri et al., 2011). Certaines des stratégies proposées se reposent sur les distributions globales de niveaux de gris via les histogrammes, d'autres exploitent des propriétés locales comme la texture, alors que d'autres intègrent des mesures d'entropie locales (Hung et al., 2019).

L'une des approches classiques pour segmenter une image en deux classes consiste à chercher un seuil de séparation. Les méthodes de seuillage global calculent la répartition des niveaux de gris et choisissent une valeur pour définir la frontière entre objets et arrière-plan (Otsu, 1979). Une fois le seuil trouvé, chaque pixel est affecté à la classe correspondant à sa position par rapport à ce seuil. D'un point de vue pratique, ce type de procédé convient particulièrement lorsque l'histogramme de l'image présente une distribution relativement bimodale, ce qui est souvent le cas dans des images où le contraste entre deux zones est marqué. Dans des contextes variés (photos aériennes, documents scannés, images industrielles), cette forme de segmentation demeure une référence, car elle s'avère à la fois rapide et facile à mettre en œuvre.

Au-delà du seul critère basé sur l'histogramme, un intérêt majeur consiste à intégrer l'analyse de la texture dans la démarche de segmentation (Hung et al., 2019). Celle-ci vise à caractériser les régularités et motifs dans la répartition spatiale des niveaux de gris : co-occurrence de Haralick, transformées en ondelettes, filtres de Gabor ou encore histogrammes de motifs. Lorsque certaines régions partagent un même histogramme global mais diffèrent par leurs structures internes, la texture fournit alors un critère discriminant supplémentaire. Si besoin, il est également possible de combiner un seuillage général à une analyse texturale pour mieux séparer les zones dont l'aspect est plus complexe. Parmi ces méthodes exploitant la texture, des stratégies entropiques ont été proposées, où la mesure de l'entropie locale, associée à un classifieur supervisé ou non supervisé, vient guider la définition de frontières entre différentes régions (Barbieri et al., 2011). Dans la pratique, une telle intégration permet souvent d'obtenir de meilleures performances globales, en particulier lorsque les zones complexes ou faiblement contrastées se voient mieux différenciées, et l'on parvient à identifier les objets d'intérêt même en présence d'un bruit modéré (Hung et al., 2019).

Il a été montré que dans de nombreux cas la robustesse de ces techniques demeure satisfaisante, tout en encourageant l'utilisation de stratégies hybrides lorsque la scène présente différents degrés d'hétérogénéité (Xu et al., 2011). Les algorithmes de segmentation modernes cherchent à fusionner un critère global (tel qu'un seuillage par méthode d'Otsu) avec des indices additionnels (contrastes locaux, entropie), offrant ainsi une segmentation plus robuste et plus précise pour un large éventail d'applications possibles (Otsu, 1979; Xu et al., 2011).

CHAPITRE 2

DETECTING WATER SEEPAGE WITH DRONE-BORNE THERMAL AND VISIBLE IMAGING: A PROMISING APPROACH FOR ENVIRONMENTAL MONITORING

Basile Lallement[1,2], Michel Baraer[1,2], Vincent Cloutier[3,4], Eric Rosa[3,4]

[1] Département de génie de la construction, École de Technologie Supérieure,
1100 Rue Notre-Dame Ouest, Montréal, Québec, Canada H3C 1K3
[2] Geotop, 201 Avenue du Président-Kennedy, Montréal, Québec, Canada H2X 3Y7
[3] Institut de recherche en mines et en environnement, Université du Québec en Abitibi-Témiscamingue, 445 Boulevard de l'Université, Rouyn-Noranda, Québec, Canada J9X 5E4
[4] Groupe de recherche sur l'eau souterraine, Université du Québec en Abitibi-Témiscamingue, 341 Rue Principale Nord, Amos, Québec, Canada J9T 2L8

Article soumis pour publication à la revue « *Remote Sensing of Environment* »,
Mars 2025.

2.1 Abstract

This study presents a comprehensive approach to detecting seepages and wetland areas at the Quémont 2 mine tailings site using drone-based thermal and visible imaging. The methodology integrates several image processing techniques, including the use of primary and secondary rasters, such as visible NDVI (vNDVI), slope, and shade layers, to eliminate false positives and ensure accurate identification of water-related features. The data collected during the drone flights were processed to highlight areas with significant thermal contrast, indicative of water seepage, while filtering out other potential thermal anomalies like vegetation and shadows.

By incorporating a hydrological analysis through drainage network simulation, the study attempts to contextualize the detected seepages by identifying possible sources of flow and distinguishing between surface runoff and underground resurgences. The methodology is presented as adaptable and cost-effective, suitable for environmental monitoring across

various industries, though it faces challenges such as sensor resolution limitations and environmental dependencies, which can affect the accuracy of results. Despite these limitations, the study shows that the combined use of thermal and visible imaging, along with advanced image processing techniques, provides a valuable tool for monitoring complex environments like mine tailings ponds.

Looking ahead, the study suggests potential improvements such as integrating machine learning models for better filtering and precision, as well as incorporating geophysical techniques to refine the hydrological analysis.

2.2 Introduction

Amid escalating climate change and resource scarcity, societies face new challenges in sustainable resource management, environmental risk prevention, and public health protection. This context underscores the growing need for cost-effective and efficient remote sensing techniques for environmental monitoring. In the shift toward sustainable practices, the mining industry is among the sectors most in need of efficient tools for environmental monitoring (Song, Song, Gu, & Li, 2020). Mine tailings, in particular, are exposed to various external factors such as wind, frost, snow, and liquid water percolation potentially enhancing the contaminant mobility (Kossoff et al., 2014).

Over time, water is likely to weaken the structures of the containment dikes, encouraging the transport and diffusion of mining waste in the environment (Ghomshei & Allen, 2000). Exudates from mine tailings, in the form of acid mine drainage, are considered one of the major sources of water pollution in many countries. They carry toxic metals in given speciation and physico-chemical forms which highly influence their toxic effects (Jonnalagadda & Rao, 1993; Chen et al., 2021). In this context, it is particularly important to be able to detect potentially contaminated water exfiltration from mine tailing structures. Seepages in mine tailings or other retaining structures are typically captured by channelling the water into seepage collection systems (Yasuda, Thomson, & Barker, 2010). This technic offers the advantages to prevent the collected water to contaminate the environment and to gauge the volumes lost through the retaining structure. On the other hand, collectors only provide monitoring of the bulk leakages volume and excludes unrecovered seepages that flow under the dam (Ben Abdelghani, Aubertin, Simon, & Therrien, 2015; Navarro-Ciurana et al., 2023). The use of geophysics to detect and quantify seepages in and underneath retaining structures has been proven being of great interest. Indeed, geophysical technics such as electrical resistivity tomography (ERT) (Moreira et al., 2022; Jian et al., 2024) and ground penetrating radar (GPR) other used individually (Poisson, Chouteau, Aubertin & Campos, 2009) or combined with other methods such as self-potential (SP), multichannel analysis of surface waves (MASW) (Adetokunbo, Ismail, Mewafy, & Sanuade, 2024), seismic refraction or electromagnetic method (EM) (Lachhab et al., 2020) have shown great potential in monitoring potentially contaminated outflows from mine tailing. However, geophysics applications to large retaining structures face challenges related to spatial resolution, penetration depths and skilled personnel availability (Pazzi, Morelli, & Fanti, 2019) that limit their large-scale deployment. The need for a combination of geophysical techniques to characterize the subsurface with an acceptable level of uncertainty makes it expensive and highly time consuming (Schrott & Sass, 2008).

Thanks to technological advances over the last few decades, numerous remote sensing techniques have emerged as fundamental tools in environmental monitoring. The development of increasingly powerful and reliable Unmanned Aerial Vehicles (UAVs) has opened the way to new scales of data (Whitehead & Hugenholtz, 2014). Equipped with thermal sensors or multispectral cameras, UAVs are now capable of obtaining aerial images used to produce high-definition maps of relative surface temperature data or to calculate indices such as the Normalized Difference Vegetation Index (NDVI) wildly use in environmental and agricultural sectors (Baluja et al., 2012; Zhang, Wu, Zhang, Jiao, & Li, 2012; Anderson et al., 2008). Drone born imagery is currently integrated into image analysis processes, using or not Artificial Intelligence (AI), for image segmentation, texture analysis or object detection (Blaschke et al., 2000; Bharati, Liu, & MacGregor, 2004; Hung, Song, & Lan, 2019; Xu, Xu, Jin, & Song, 2011). For leakage or seepages detection, Infrared

Thermography (IRT) gradually arises as one of the best Non Destructive Testing (NDT) technic (Garrido, Lagüela, Otero, & Arias, 2020; Deitchman & Loheide II, 2009). This is especially true in contexts where the background surfaces are relatively homogeneous such as concrete dams or levees (Li et al., 2024; Thomson et al., 2015). In those contexts, the use of complex AI algorithm helps to automatically identify dam-surface seepage from thermograms collected by an UAV carrying a thermal imaging camera. Compared with the visible light recognition method, the infrared thermal imaging technology can identify the location and scope of leakage hazards especially at night (Wang, Liang, & Rongliang, 2024). Studies conducted on real retention structures underline the versatility and high-resolution data acquisition capacities of modern commercial UAV equipped with IRT cameras (Llerena & Sattarvand, 2023). On the other hand, more complicated environments, such as several decades old mine tailing dikes, still require methodological and/or technological improvements to efficiently detect minor leakages or seepages. Vegetation, complex backgrounds, low signal-to-noise ratio and poor thermogram resolution impose significant adverse effects on automated results (Wang et al, 2022). In those environments thermal images interpretation is still limited by diverse factors including technical issues of image acquisition, diurnal changes in radiation and temperature, and rock face heterogeneity (Pandey, Gleeson, & Baraer, 2013; Mundy, Gleeson, Roberts, Baraer, & McKenzie, 2017).

In those context actual deep-level image processing and machine learning shows limits in accurately identifying the hidden dangers (Wang et al., 2024). Recent research efforts address those concerns by focusing on improving machine learning algorithms on photogrammetry based thermal models to identify leakages (seepage) in damming structures (Gomez Llerena, Ghahramanieisalou, & Sattarvand, 2023; Llerena & Sattarvand, 2023). Alternatively, progresses can be made by increasing the number of components used for AI application in remote sensing for environmental monitoring (Janga, Asamani, Sun, & Cristea, 2023; Khonina et al., 2024). The challenge lies in generating multiple rasters of interest while using a single data source and minimizing data acquisition time.

Here, we explore this approach by proposing a combination of primary and secondary rasters generated using a drone-based dual thermal and visible camera. We operate in a large, complex, challenging more than 40 years old multi-level mine tailing site during daytime to meet conditions met in real mining regions of the world. By adding primary and secondary raster to the treatment process the aim is to open new avenue for complex AI algorithm development. The objective of the study is therefore to identify raster's that can be extracted from TIR and RBG images collected from a unique commercial dual camera mounted on a UAV. Tested rasters are computed from published algorithm selected based on known obstacles to leakage detection in complex environments: vegetation, shadow and puddle.

2.3 Material and methods

2.3.1 Study area

The study was conducted at the Québec 2 tailings pond, located in Rouyn-Noranda, north-eastern Quebec (Figure 2.1.A). The site that spans an area of 102 hectares, is owned and managed by the Horne smelter, a Glencore company. Until recently, Quemont-2 collected mine tailing from foundry by co-sedimentation of wet mud. Quémont 2 is in operation since the 80th and has developed into two phases. A first pond was created (Figure 2.1.A) over soils and fractured bedrocks by building 3 dikes: dike D (Figure 2.1.B), dike E (Figure 2.1.C) and dike F (Figure 2.1.D) at its west. Once filled, another dike (G), south- southwest/north-northeast oriented was built on top of the phase 1 deposits. As a result, since 1995, dike G separates the site in its actual configuration into an area called the "old" park at the west and another one named the "new" park in the east (Figure 2.1.A). Dike G is made of granular materials without any clay core. Its structure thus makes it permeable and facilitates water through-flows from the "new" park to the surface of the "old" park. The original dikes, D, E and F are cored by clay like materials to minimize water seepages. They were built over a shallow clay deposit and a fractured bedrock (El Mrabet, 2021). A pond is kept unfiled by residues at the extreme east side of the mine tailing. It is used to monitor the water table in the residue and, when needed, to pump water to a treatment plant.

With age, the site shows several leakages/seepages in its west, downstream of the dikes D, E and F. An initial site visit revealed a substantial wetland at the residues surfaces in the “old” park at the base of the G (Figure 2.1.E). Another wetland was observed downstream of dike E (Figure 2.1.F). Both wetlands were characterized by the presence of dense vegetation. The wetland at the surface of the “old” park formed a streamlet at its southern extend that crossed dike D at several locations. Distributed seepages converged to form several streamlets flowing down westward and then southward at the base of the old dikes. The most important streamlet formed at the southernmost extend of the wetland on the “old” park and flowed down over dike D in its middle (Figure 2.1.G). Additional streamlets were observed forming at the base of dikes D and E (Figure 2.1.I) where very fine flow, almost akin to dripping, emerging from rock.

Further downstream most of the streamlets appearing at the base of the dikes merge to form a stream heading to a retention pond situated outside Québmont 2, in its southwest. A couple of streamlets drained toward the northwest too. Most of the seepages and streamlets showed red / oranges colors deposits in their direct vicinity.

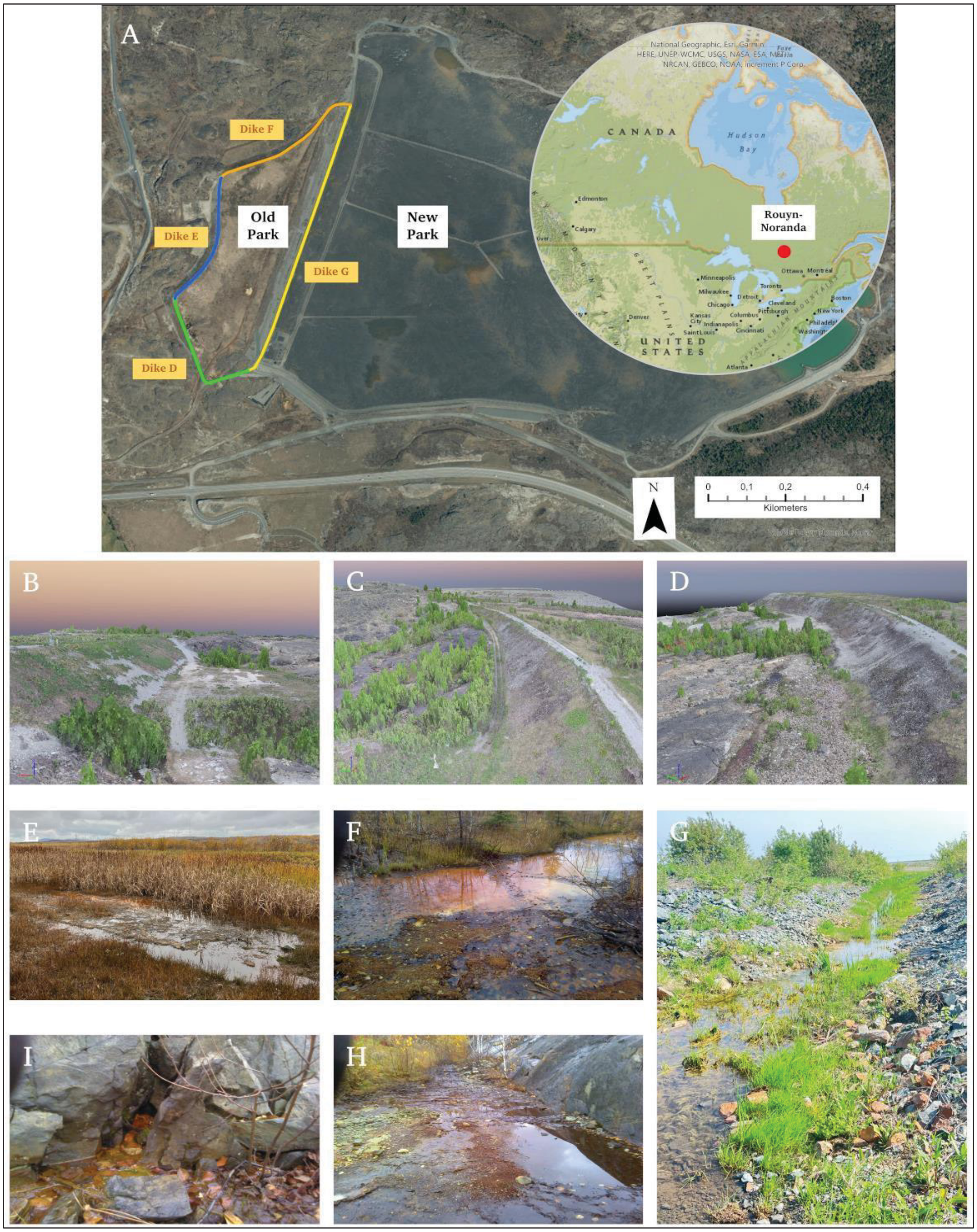

Figure 2.1 Maps and images of the study area. (A) Map representing the study area, with the locations of the dikes and the two parks of the site. (B-D) 3D representation of dikes D (B), E (C), and F (D), generated by Pix4Dmapper® (Pix4D SA, 2022, version 4.8.1). (E-I) Images of seepages and wetlands observed on the site

The site is surrounded by a natural environment featuring extensive vegetation cover. A recent study based on the site water budget estimates the site total water loss by seepages leaks and transfer to the aquifer at around 3 000 m^3 per day (Mhiri, 2023). Based on the initial observations, we identified three different zones for conducting drone based thermal and visual surveys with the objective of detecting seepages and outflows from Quémont 2 dikes (Figure 2.2.A). Zone 1 (Figure 2.2.B) was used for a first calibration of the image processing parameters, zones 2 (Figure 2.2.C) and 3 (Figure 2.2.D) were used to evaluate the robustness of the proposed methods with no further parameter adjustments. Ranging from 55 to 88 hectares, each zone is of industrial dimension. Zones share similar elevation ranges but differ in orientation, slopes, vegetation covers and micro topography.

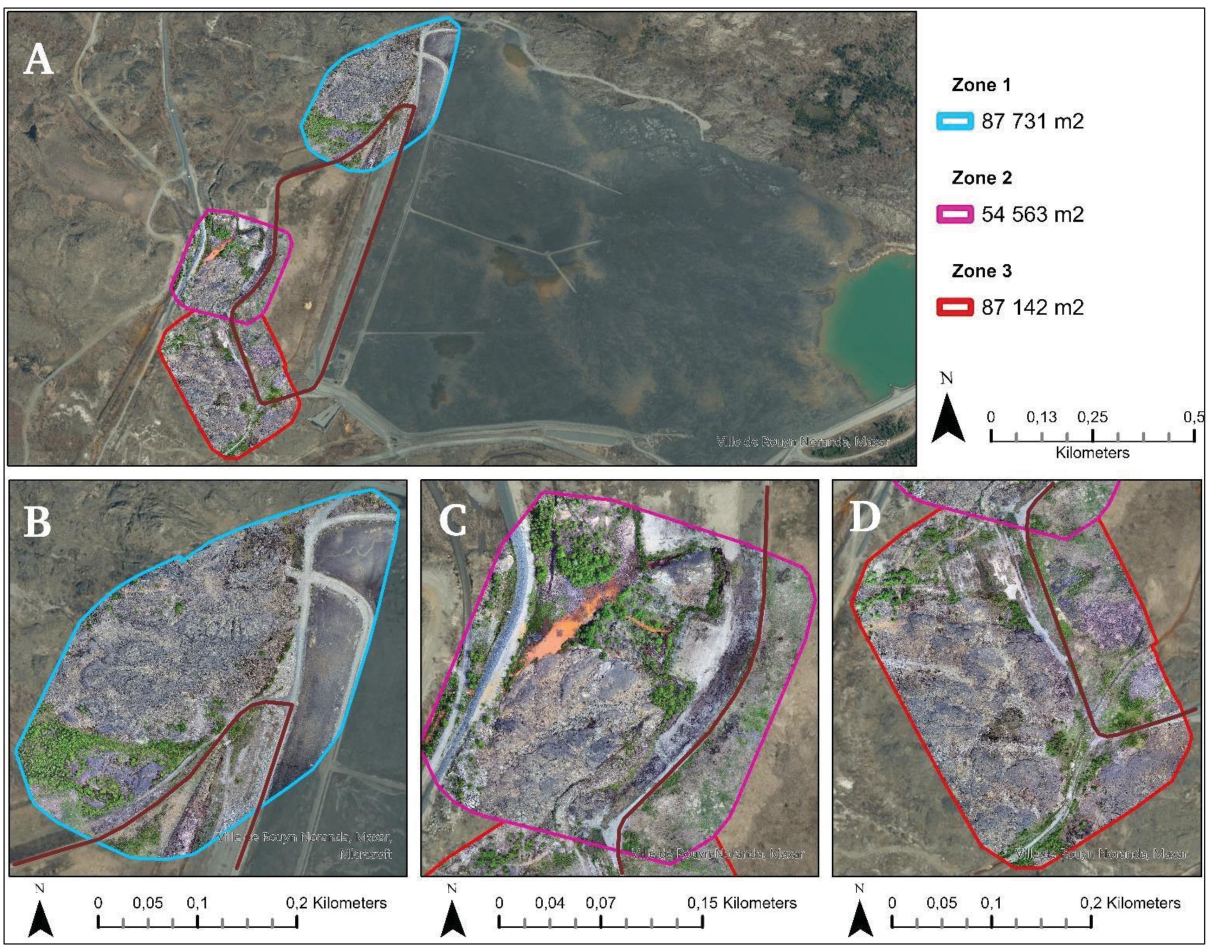

Figure 2.2 (A) Overview of the three zones of study with their areas and the location of the dikes. (B-D) Zooms on zone 1 (B), zone 2 (C), and zone 3 (D)

2.3.2 Materials and data acquisition

We used a DJI Matrice 200 drone which is mounted with a Zenmuse XT2 payload that has a visible RGB camera and a FLIR T thermal sensor to capture images in both visible and IR spectrum (Figure 2.3). The visible camera captures high-resolution images up to 3840×2160 pixels, with a 1/1.7" CMOS sensor and a 25 mm lens. In contrast, the FLIR T thermal sensor offers a much lower resolution, shooting images at 640×512 pixels and operates within a spectral range of 7.5 to 13.5 μm. This equipment provides the advantage of optimizing the flight durations by capturing images in both visible and IR spectra in one flight and hence making the subsequent data processing phase much easier.

Figure 2.3 Images of the unfolded DJI Matrice 200 drone, its control remote, and the Zenmuse XT2 payload, pairing a visible camera and a FLIR T thermal sensor

All flights are created with the DJI Pilot application. The flight plan for each zone is a double grid pattern, with a flight altitude set at 100 m above takeoff elevation, 90% overlap, and a camera angle of 90° (Table 2.1). On June 2, 2022, drone flights are performed over the three zones in favorable flying conditions, targeting a strong temperature contrast between the water and the ground. Georeferenced images from the drone are collected for data acquisition over the different zones (Figure 2.2). To minimize the effects of other external factors, such as weather conditions, or light levels, each flight was performed at close intervals to ensure that the data gathered from each zone was uniform and comparable.

Table 2.1 Drone flight conditions for each zone

Zone	Start Time LST	End Time LST	Temperature (in °C)		Sun elevation (in °)		Solar azimuth (in °)		Relative humidity (in %)	Wind speed (km/h)
			Min	Max	Min	Max	Min	Max	Mn	Mn
1	7:55 AM	8:28 AM	12,9	14,1	23,1	28,6	82,0	87,9	71	8
2	9:31 AM	9:46 AM	14,0	14,2	39,0	41,4	100,2	103,4	62	8
3	11:21 AM	11:50 AM	14,9	16,2	55,6	59,1	129,1	139,8	57	5

2.3.3 Methods

2.3.3.1 Method overview

Water detection strategy, both in seepages, streamlets and wetlands, is based on the heat contrast that exists between water and its surroundings (Mundy et al., 2017). The efficiency of capturing meaningful thermal images depends on the temperature contrast between the ground surface and that of water. In daytime, in the study measurement conditions, groundwater is expected to be significantly colder than the surrounding. Although the absolute stream temperatures on non-corrected IRT images may deviate from true temperatures, contrast with the surroundings remains as we move downstream from sources at the study scale (Baker, Lautz, McKenzie, & Aubry-Wake, 2019). IRT has been shown to be adapted to study targeting of areas of groundwater seepage at the surface (Ozotta & Gerla, 2021). However, since water is not the only feature that creates a thermal contrast with the surroundings, IRT images need to be filtered to avoid false positives water detection (Morgan & Colins, 2022). The primary sources of temperature contrast other than water include vegetation (Luquet et al., 2003; Still et al., 2019), shades (Chaudhary & Chaturvedi, 2017), slopes (Frodella, Gigli, Morelli, Lombardi, & Casagli, 2017), and cracks (Yang et al., 2019). Vegetation, shading, and slope effects are filtered using visible images as a primary raster (Figure 2.4). In the pre-processing phase visible orthomosaics are processed to generate vNDVI indexes (Costa, Nunes, & Ampatzidis, 2020), shade and slope layers. Slope and shading layers both produced from a DTM, as an intermediate layer between the visible mosaics and these three secondary rasters (Figure 2.4). vNDVI allows estimating the NDVI index without using a multi-spectral camera. The use of vNDVI is of great interest as a number of commercial drones propose visual–thermal dual cameras in a single payload and a multispectral camera in another payload. The thermal layer was simply produced by aggregating IRT images.

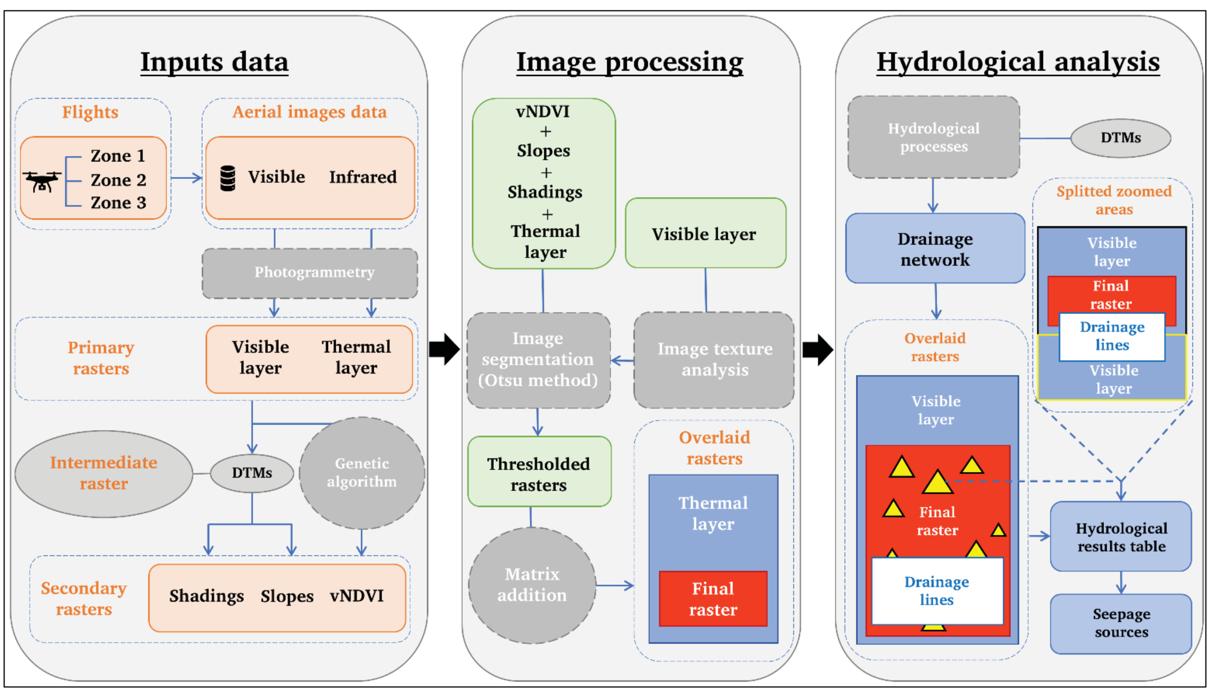

Figure 2.4 Method overview

Image processing consisted in creating a false positive filtering raster by applying thresholds to the three secondary rasters and to the primary thermal layer. A fifth raster also representing false positives is generated using another analytical method, image texture analysis (Barbieri, De Arruda, Rodrigues, Bruno, & da Fontoura Costa, 2011). The method used aims to calculate local entropy measures to quantify textural irregularities for each group of pixels. The image cut into several groups of pixels are then compared closely according to their local entropy value and classified according to their similarity. This process also integrates a segmentation process that allows to filter only the groups whose entropy differentials are the highest, indicating a high textural irregularity between two neighboring groups of pixels. These filtered texture breaks then make it possible to distinguish the surface water areas from the rest of the soil elements such as vegetation or rocks. The aim here is to eliminate spots where the targeted temperature contrast and physical characteristics arise from non-water-related features. By adding together the three secondary thresholded rasters, the thresholded texture analysis layer and the thresholded thermal primary raster, we obtain a final raster showing spots of thermal contrast associated with the presence of water only. The last stage consists in differentiating minor seepages and outflowing water from significant primary water sources. This is done by identifying the lines of lowest points in topographical valleys. Hypothesis is made that substantial leakages generate perennial streamlets which head points are of primary interest for environmental site monitoring. The site drainage network is calculated from the DTM.

2.3.3.2 Pre-processing

2.3.3.2.1 Primary rasters

The two primary rasters are created in the form of orthomosaics in visible and infrared spectrums. The primary visible raster is composed of raw .jpg images that are imported into Pix4DMapper® (Pix4D SA, 2022, version 4.8.1) and converted to orthomosaic using high processing settings for point cloud densification and DTM generation. Upon calculations and software analysis, the result yielded, for each zone, a visible raster with three bands - red, green, and blue, and a DTM as an intermediate raster. The IR orthomosaic map is generated by the engine software Open Drone Map (ODM), an open-source toolkit that offers a cloud-based application to support the processing of aerial imagery (Ampatzidis, Partel, & Costa, 2020). The user interface WebODM® (OpenDroneMap, 2022, version 1.9.16) allows connection to the processing node hosted on a dedicated server and enables the import of the TIR image datasets into the software in .RJPG format. This image format includes radiometric data embedded in the image's metadata which is specifically suited for thermal analysis projects. The processing workflow settings selectable in the WebODM® interface are configured according to the software's default values. The rasters resulting from the WebODM® and Pix4DMapper® (Pix4D SA, 2022, version 4.8.1) processes are then exported in raw .GeoTIFF format to preserve the radiometric metadata and georeferenced data, facilitating the georeferencing correction. The primary rasters are then imported into ArcGIS Pro® (Esri Inc., 2023, version 3.1.3), a Geographical Information System (GIS) software. The IR orthomosaic containing the soil relative temperatures values at each pixel on the map needs to be standardized according to the values of the upcoming secondary rasters. The raster first undergoes a conversion to a shade of gray using the Grayscale function in the Raster Functions toolbox of ArcGIS Pro®. The raster's values are finally normalized based on a linear normalization process with the Raster Calculator toolbox to obtain a scale of values between 0 and 1. A value scale common to all the rasters will subsequently allow perfect compatibility for the superposition of rasters by matrix addition operation.

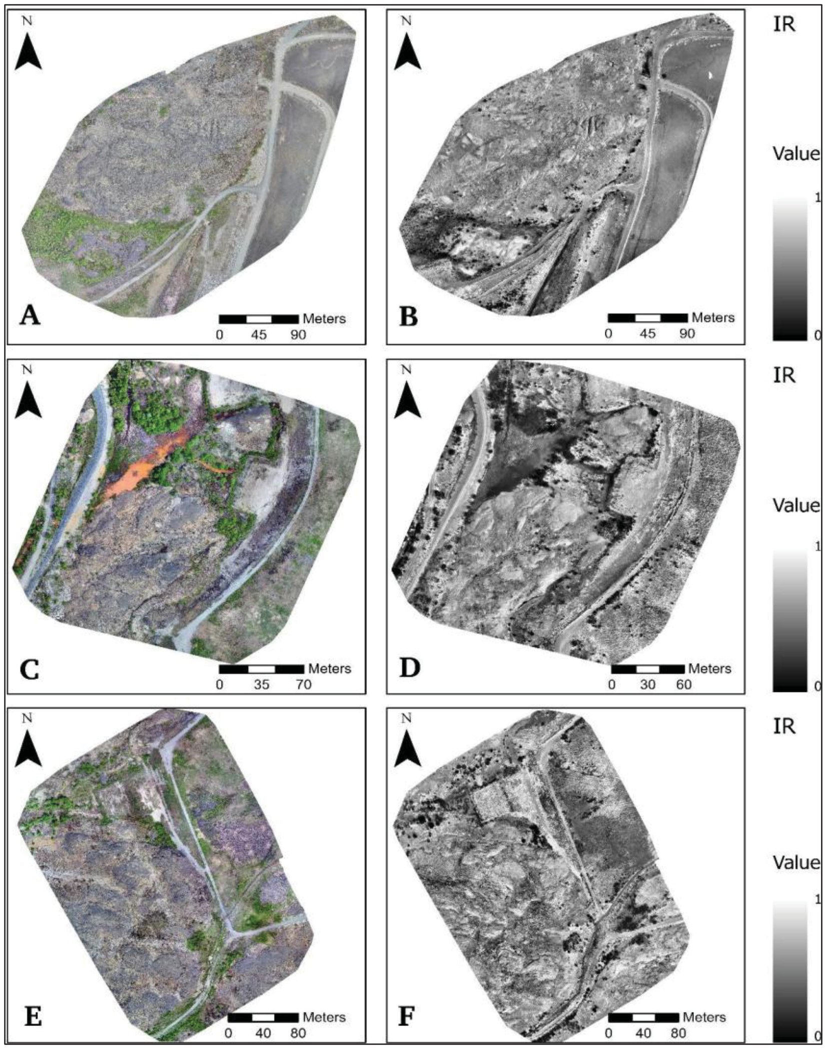

Figure 2.5 Primary rasters representing orthomosaics of visible (A, C, E), and IR (B, D, F) for each zone, respectively zone 1 (A, B), zone 2 (C, D) and zone 3 (E, F)

2.3.3.2.2 Georeferencing and DTM corrections

Once imported and processed by the ArcGIS Pro® software, the primary rasters and DTM are overlaid on the basemap World Imagery. The DTM raster must be corrected owing to the presence of dense vegetation. To prepare the raster for corrections, the Calculate Statistics function is used to ensure the minimum and maximum elevation values for subsequent operations. The DTM correction begins by inverting the raster using the Raster Calculator tool in the Analysis tab by multiplying the raster values by -1. This operation inverts the values of each pixel so that the elevation peaks due to vegetation become inverted basins. These basins are then filled using the hydrological tool Fill contained in Spatial Analyst Tools. The filling process fills the inverted basins as well as the no-data pixels by interpolating the values from the neighboring values. The raster is inverted again using the Calculate Statistics function to obtain the final DTM and exported in .TIFF format. Given that the raw data that contributed to the creation of the two rasters originated from two distinct cameras, and that the primary rasters themselves are products of two disparate software platforms, a misalignment and distortions might emerge. The discrepancies observed with the overlay of the two primary rasters and DTM are corrected using the georeferencing tools available in ArcGIS Pro®. The Imagery tab in the software provides access to the Georeferencing tool, which allows to manually Add control points. For each zone, at least three easily recognizable geographic reference points are defined, identifiable on the three raster sources (primary and DTM), preferably along the map edges and in the center. These points are manually mapped onto each raster across all zones. With the Auto apply option enabled, the transformation and corresponding correction are updated after each added point. Once all control points are defined and the alignment corrected, the secondary and intermediate rasters are finalized, as shown in Figure 2.5. Normalized thermal orthomosaics show a high level of contrast that aligns with the research objectives, while the visible orthomosaics reveal a very contrasted landscape characterized by dense vegetated areas and bare soils.

2.3.3.2.3 Secondary rasters

Two secondary rasters, slopes and shadings, are both created from the DTM layer, using the Spatial Analyst Tools of the Geoprocessing toolbox in ArcGIS Pro® software. The Slope tool set according to the default values allows to convert the DTM raster into a new raster representing the slope at each cell of the map. To generate the secondary raster of the shadings, the Hillshade tool is used, also available among the Spatial Analyst Tools, from the initial DTM raster. The tool is configured according to input values before being launched, in order to take into account the position of the sun during drone flights, and thus attempt to simulate the shadings as close as possible to real field conditions. Thus, the sun azimuth degree and the sun elevation degree are entered in the parameters, following the values presented in Table 2.1. After running the Geoprocessing tools, we obtain the first two secondary rasters which are also exported in .TIFF format. The third secondary raster to generate is the vNDVI indice from the visible primary raster. This part of the process is done with the image processing algorithm integrated into ODM via the WebODM® user interface (Ampatzidis et al., 2020). The visible images are imported into the interface and the processing parameters are filled in according to the default settings before launching the process. Once the orthomosaic is generated, it is then possible to choose to apply the vNDVI index among those available. The orthomosaic is then converted and the vNDVI values can be read at each cell of the map. The vNDVI values are calculated from the red (R), green (G) and blue (B) values included in each pixel of the visible orthomosaic, following an equation developed according to a genetic algorithm, in order to predict the best possible solution for calculating the vNDVI index (Costa et al., 2020). The vNDVI has been shown to have high accuracy in estimating values, with an average error of 6.89%, making it a robust alternative to multispectral cameras for obtaining an NDVI index.

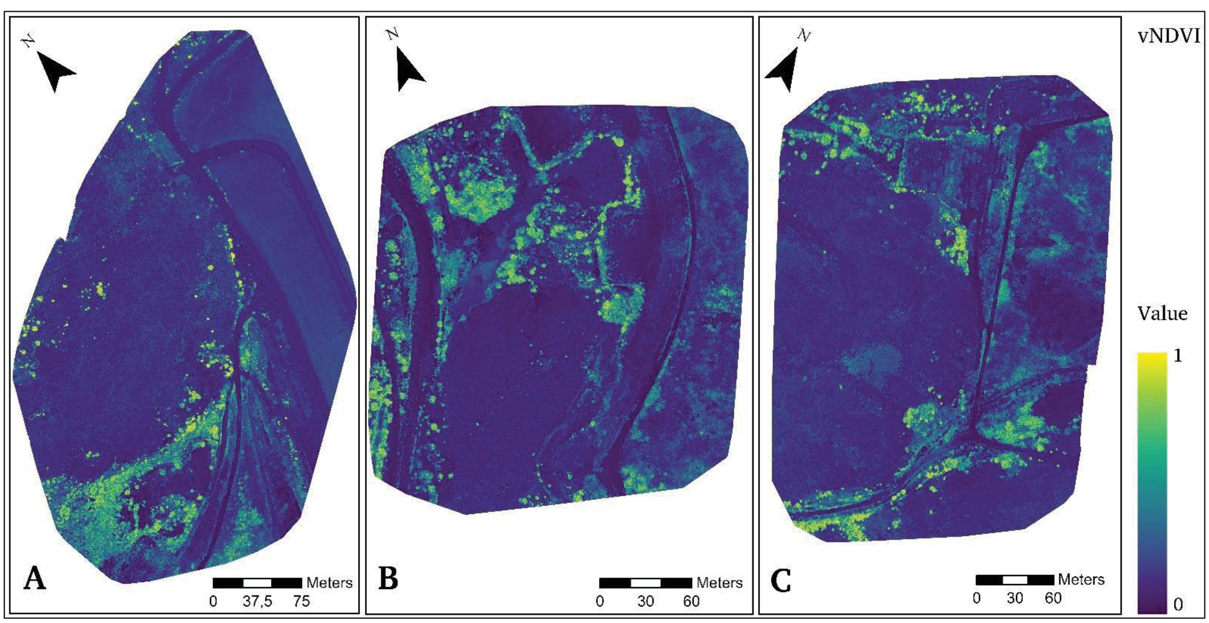

Figure 2.6 Orthomosaic of the vNDVI indice for zone 1 (A), zone 2 (B), and zone 3 (C)

Before exporting the final vNDVI raster, it is possible to choose the minimum and maximum possible values by observing the histogram of the distribution of the values, to eliminate the extreme values that are too far apart and increase the final contrast. Once the desired parameters are set, the vNDVI orthomosaic is then exported in .GeoTIFF format and imported into ArcGIS Pro® to undergo a final normalization step so that the values are no longer between -1 and 1 as are the vNDVI and NDVI values, but between 0 and 1. From a single visible orthomosaic layer, we obtain three secondary rasters to be integrated into our image processing step, in addition to the primary thermal raster. Figure 2.6 presents the vNDVI secondary raster for each zone, showing the localization of many vegetation areas on the map, with precision and a high contrast.

2.3.3.3 Image processing

2.3.3.3.1 Image segmentation

Once the IR primary raster and the secondary rasters are generated, they are converted into grayscale through the Grayscale function in the Raster Functions toolbox in ArcGIS Pro®. The secondary rasters of vNDVI, slopes, shadings, as well as the primary thermal raster are then used for the image segmentation process. Segmentation by binary classification is performed using the Otsu method (Otsu, 1975; Hung et al., 2019; Xu et al., 2011) with the matrix calculation tool Binary Thresholding function in the Raster Functions toolbox integrated into ArcGIS Pro®. The thresholding calculation according to Otsu is based on the analysis of the gray level histogram of each raster to deduce an optimal threshold. It aimed at maximizing the separability of pixels into two distinct classes of values (0 and 1), while minimizing the intra-class variance and maximizing the inter-class variance. Thus, the segmentation will separate the sought-after information from the background for each raster. Once the binary rasters created, it is necessary to assign a value to the elements of interest in the study, water seepages, and to keep this value for all of the binary rasters until the final raster. The value chosen for water is here defined by 0. By proceeding in this way, when we superimpose the rasters by matrix addition, only the values of interest 0 corresponding to water will be filtered and kept in the final raster. Finally, to know if the 0 values of the binary rasters correspond to water observed in the field, the binary rasters are compared to the visible orthomosaic in order to check the geographical points whose presence of water has been verified on the day of the drone flights. Four new thresholded rasters are generated as merged in Figure 7 for each zone. If we rely on the raster of zone 1 after segmentation, we can already see that many 1 values from the vNDVI, slopes and shadings rasters (Figure 2.7.B,C,D) correspond to some of the 0 values contained in the IR raster (Figure 2.7.A). For example, the vegetation index showing vegetation patterns appear to coincide with certain patterns appearing in the IR raster.

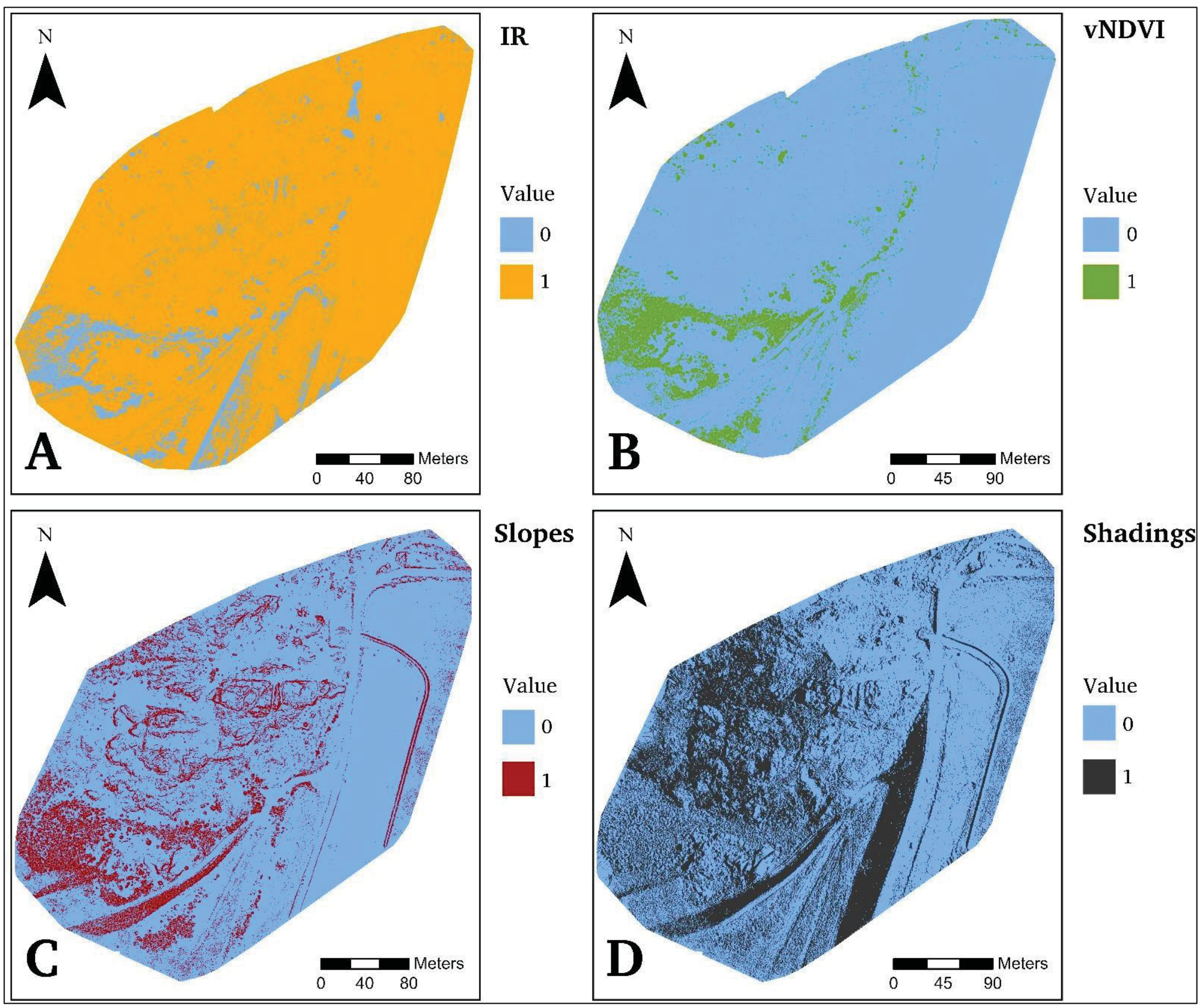

Figure 2.7 Primary and secondary rasters after image segmentation process for the first zone. Each raster is converted into binary values, with 0 indicating the probable presence of water and 1 indicating the probable false positives. (A) IR thresholded raster

2.3.3.3.2 Image texture analysis

Before merging the final raster, a last complementary raster must be generated. An image texture analysis provides an additional filtering criterion by highlighting the highest texture differences between groups of neighboring pixels. These textural breaks appear as a significant change in element class, for example from vegetation or rock to water. This process needs the visible orthomosaics for each zone and be imported from ArcGIS Pro® to MATLAB® (The MathWorks, Inc., 2022, version R2022b) software with the .TIFF format, conserving meta datas and georeferencing.

The Image Processing Toolbox is needed to use the Texture Analysis tool with MATLAB®. After importing the rasters, the input data must be read using the "imread" command. The next step is to create a texture image by executing the "entropyfilt" command to generate an array where each output pixel represents the entropy value of the 9-by-9 neighborhood surrounding the corresponding pixel in the original grayscale primary rasters. The "rescale" command is then used on each of the results ensuring that pixel values are in the range [0, 1], as expected for all the rasters of the study.

The last step is creating a thresholded raster from the rescaled raster using the "imbinarize" command. Unlike Otsu's thresholding method built into ArcGIS Pro®, this command allows you to manually set a threshold value. This flexibility is particularly useful in this study, due to the fundamental differences between texture analysis entropy calculations and the thresholding method used by ArcGIS Pro®. Otsu threshold method automatically determines a single threshold by analyzing the overall grayscale histogram of the image, which may not be optimal for images with significant local variations. Conversely, local entropy measurements from texture analysis process are calculated on 9x9 pixel matrices and compared progressively, allowing segmentation more adapted to local irregularities. The possibility of manually setting the threshold after these local measurements thus makes it possible to preserve this fine classification of values and to avoid the generalization imposed by global thresholding applied to the entire image. By visualizing rasters of zone 1 with different values of threshold, a balance is found between the quantity of information retained and the level of detail in the observed patterns, leading to the selection of a threshold value of 0,8. In assess the robustness of the proposed methodology, this same threshold value will be applied to the texture analysis rasters of the other zones.

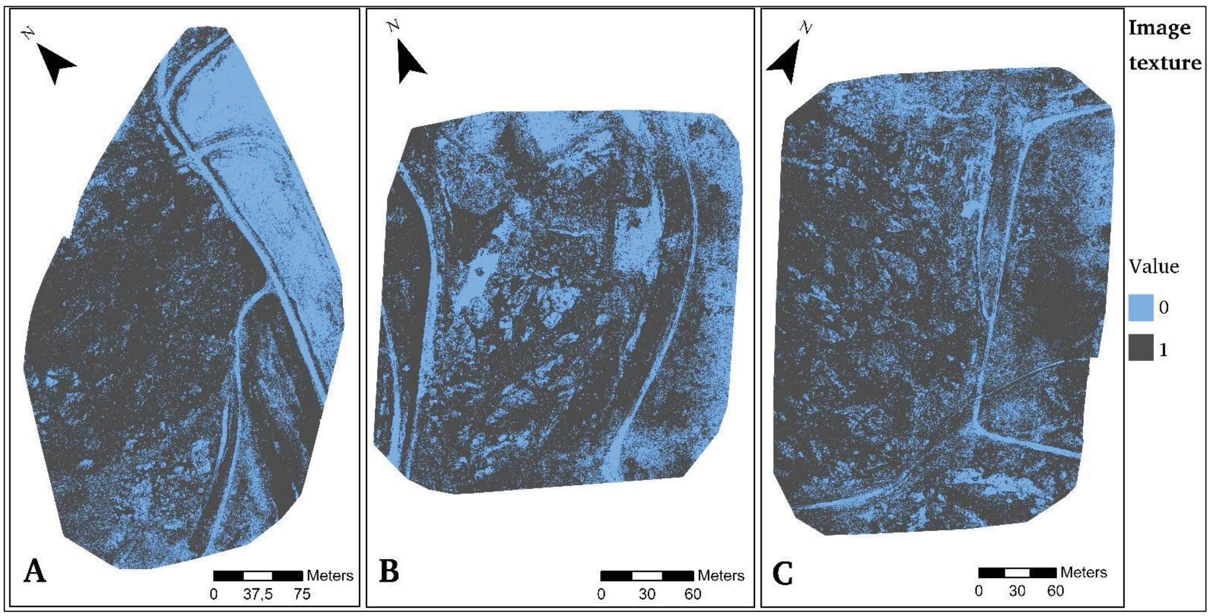

Figure 2.8 Thresholded raster after the image texture analysis of zone 1 (A), zone 2 (B), zone 3 (C). Each raster is converted into binary values, with 0 indicating the probable presence of water and 1 indicating the probable false positives

The result of this texture analysis image process provides a last raster of information, representing the distribution map of areas likely to present visual texture characteristics similar to those of water. The rasters obtained are then exported from MATLAB® while retaining the .tiff file extension, precising the code number matching with the projected coordinate system with the .TIFF original raster via the command "geotiffwrite" and imported into ArcGIS Pro®. The results merged through the Figure 2.8 show consistency between the values filtered after texture analysis and areas in the visible spectrum presenting significant visible irregularities. This is the case for vegetation or rocky areas presenting strong contrasts in topography, coinciding with homogeneous topographical characteristics of the plateaus of the upper parts of dikes D, E and F, where values have been retained in this thresholded raster from the image texture analysis process. Elements exhibiting a continuous textural regularity such as roads therefore appear in this raster which should also be the case for water flows.

2.3.3.3.3 Final raster

Each secondary thresholded rasters (vNDVI, slopes, shadings), in addition to the IR and texture image thresholded rasters are overlaid in ArcGIS Pro® to create the final raster. To achieve this, the "Raster Calculator" tool from the "Spatial Analyst Toolbox" is used to add each of the rasters together and create a final raster, as shown by the red raster in the Figure 2.9 overlaid on the IR raster. This raster shows pixels identified as surface water for the three zones of interest. Pixels that are not occurring in each raster are therefore eliminated and only common pixels are retained and contained in the final raster.

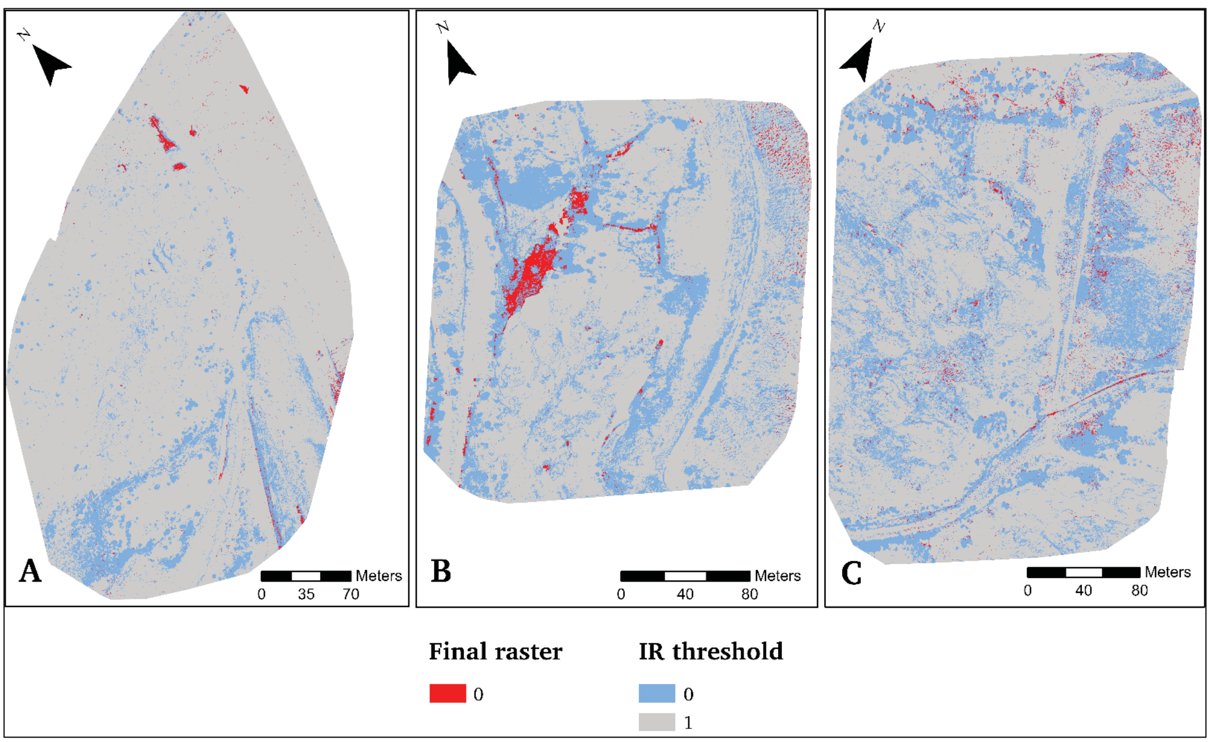

Figure 2.9 Final raster for each zone overlaid onto the IR thresholded layer. The displayed value of 0 corresponds to retained values, and the value of 1 corresponds to negative values for each associated index. (A-C) Respectively orthomosaics of rasters for zone 1,2 and 3

Those pixels appear on the final raster whatever the significance of water or source is. Pixels in red correspond to the spots of high thermal contrast as calculated based on the IR images that have not been canceled by the mask raster application. For the three study areas, we observe limited detectable zones in red, sign of a certain selectivity of the applied method. The exception made by the large area considered as water in the B zone corresponding to a marsh we observed during the site visit (Fig. 2.1.F).

2.3.3.3.4 Hydrological processes

The final raster alone therefore does not allow differentiating isolated pools from streams and from water sources. In order to support decision making we propose identifying the position of each area showing substantial water pixels concentration in the drainage network. Hypothesis is made that substantial leakages from the mine tailing complex generate runoff that feed the downstream drainage lines. Where water is detected at several sections of a drainage line, leakages origin would therefore situate in the most upstream one. Drainage networks are extracted from the DTMs using the ArcGIS Pro® hydrological tools. Thus, the DTM rasters were provided as input data to use the "flow direction" function, deducing the water flow direction for each cell comprising the raster. The "sink" identification and "fill" functions were used to correct erroneous values for cells with undefined drainage directions or those lower than all neighboring cells. Once the corrections were made, the "flow accumulation" function calculated the cumulative flow for all cells draining into each cell on a downward slope. Drainage lines were then drawn by applying a threshold to the flow accumulation raster. This was done for each zone by accepting the default value proposed by ArcGIS Pro®. As a final stage the resulting drainage network for each zone is overlaid to the visible orthomosaics and the final raster in order to visually identify spots of substantial leakage from the tailing (Figure 2.10). We here do not restrict the investigation area to the dikes or their immediate vicinity as leakages in those environments may appear in distal spots via fractures in the bedrock for example.

2.4 Results and discussion

2.4.1 Results

Figure 2.10 aims to support the hydrological analysis by superimposing the final raster with the drainage network. In order to facilitate contextualization, we choose placing the visible orthomosaics in the background. For each study zone, Figure 2.10 provides a view of the entire zone with areas of high red pixels (water) concentration delineated with a black line (left part of the figure) (Figure 2.10.1,2,3). Hypothesis is made that areas with substantial water detection are observable from the map overview. This criterion is here proposed for assessing the methodological concept only and could be questioned in real applications.

To achieve that objective, eight areas presenting the highest red pixels concentration in zone 1 were identified (Figure 2.10.1, A to H). Using zone 1 as reference, a similar number was selected in zone 2 (Figure 2.10.2, A to H) while only six areas were found in zone 3 (Figure 2.10.3, A to F). The hydrological analysis consisted first in zooming into each area to verify the presence of water in the visible orthomosaic. In a second step, the position of each area compared to drainage was qualified as follow: lower section, middle section and upper section. Where more than one area is situated on a single drainage line, those areas are considered as connected and the upper area is considered feeding the downstream ones. Those upper areas can be considered being the closest to the leakage origin. For each zone, zooms of four of those areas are displayed in the right part of Figure 2.10. In order to facilitate visual detection of water, zoomed areas of investigation are split into two parts: one with the red pixels indicating the pixels identified as water (black boxes), the other one presenting the visible layer and the drainage lines only (yellow boxes).

The results overview for zone 1 show the eight selected areas for further investigation (Figure 2.10.1). We observe that those eight areas regroup the vast majority of the red pixels of the zone. In addition, two smaller spots are visible in the top right portion of zone 1 and an area of diffuse, less concentrated red pixels in the bottom right section of zone 1 can be observed. Apart from this last area, Figure 2.10.1 suggests the selectivity of the method allowed distinctively spotting areas of interest. As summarized in Table 2, surface water was identifiable on all visible orthomosaic zooms. This is illustrated for the four examples presented in Figure 2.10.1A to 1.D. Examples 1A to 1D show four different types of surface water. 1.A area (Figure 2.10.1A) is a wetland like water accumulation area with limited signs of flow. It is free of high vegetation and situated on a relatively flat topography, without rocky obstacles that could cause shading. Figure 2.10.1A shows the final raster was able to differentiate water from the surrounding vegetation. Compared to the area 1.A, 1.B (Figure 2.10.1B) is situated in an area with denser and taller vegetation. Identifying that surface water can be seen more challenging than in 1A. This confirms the performance of the final raster to differentiate between vegetation and water, even in areas that are dominated by the vegetation. Area 1.C (Figure 2.10.1C) represents a different area from the two firsts. The area is vegetation free and dominated by apparent bedrock and numerous boulders. Detecting standing water between boulders suggests the final raster allows differentiation between shaded bedrock and water. Area 1.D (Figure 2.10.1D) represents a pool like water body located at the base of the rocky outcrops in zone 1, bordered on the east side by the G dike. Unlike the previously observed areas, the water surface area of approximately 20 m2 is not affected by cracks, shading and from any vegetation. Area 1.D appears very clearly on the final raster too. The hydrological analysis results (Table 2) show three areas identified as situated at the upper section of a drainage line. Among those three areas, two, 1.C and 1.F, situated on drainage lines that crosses other areas of identified as water in the middle or lower sections. Such upstream downstream connection confirms water accumulates and possibly flows out of the studies zones following the drainage line. Those two areas can therefore be considered as interesting targets for field investigation. Overall, the zone 1 results suggest the proposed method, at least in areas used for parametrization, allows identifications of potential active leakages from the mine tailing and provide indications on the water sources that should be targeted for field investigation.

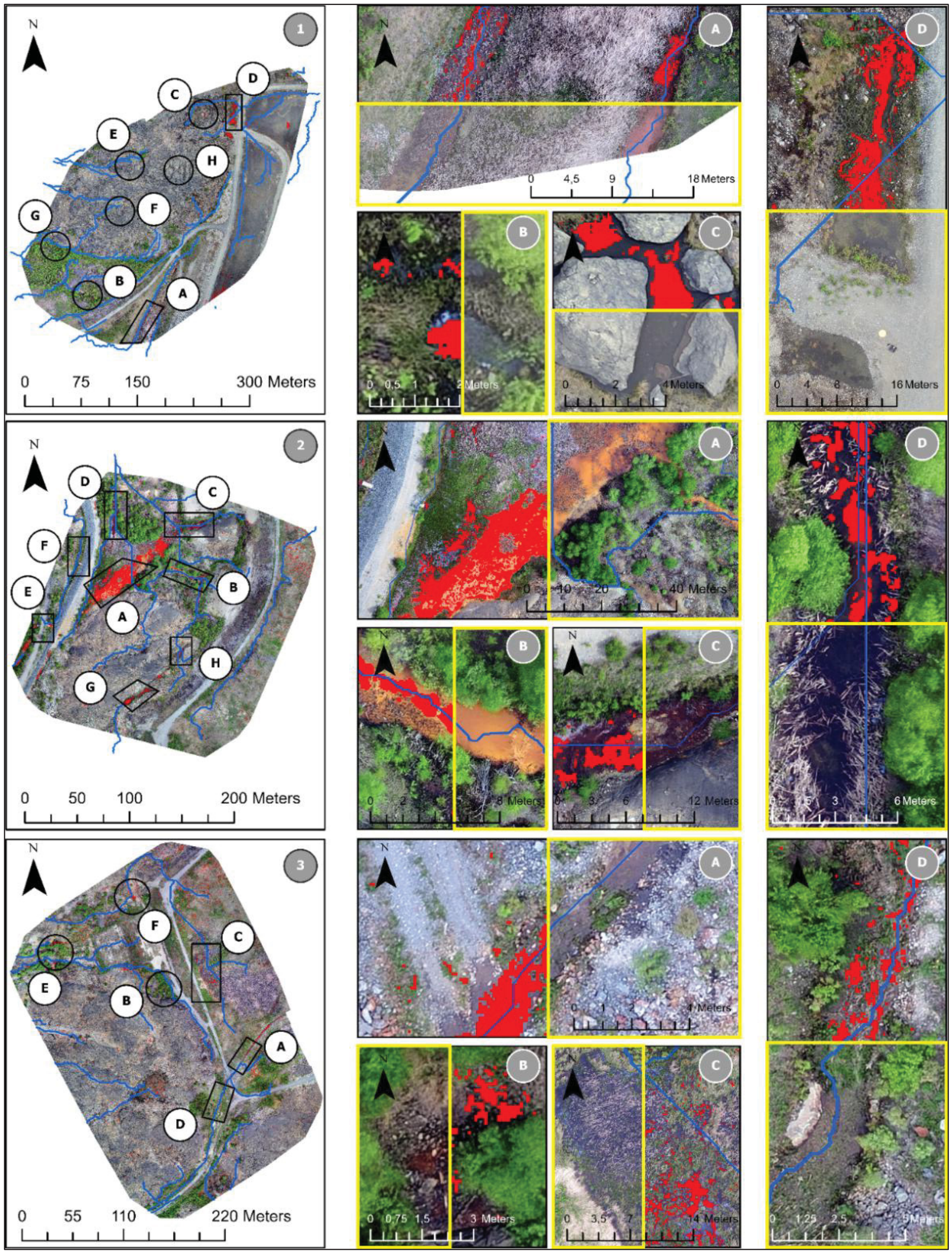

Figure 2.10 Results overview overlaying the final raster and drainage network in the foreground, and the visible orthomosaic in the background (1-3). Identified areas zooms indicated for zone 1 (1.A-H), for zone 2 (2.A-H) and for zone 3 (3.A-F). Areas in black circles are zoomed and detailed in the right part of the figure. Each area zoom box is split into two parts. Black boxes overlay the final raster, drainage network and visible orthomosaic. Yellow boxes overlay the visible orthomosaic and the drainage network only

Zone 2 was surveyed immediately after zone 1 and the analysis was performed keeping the same image texture threshold value as that first zone. Similarly to zone 1, zone 2 shows easily identified areas of high concentration of pixels identified as water (Figure 2.10.2). However, unlike Zone 1, Zone 2 exhibits a somehow noisy final raster with observable individual red pixels distributed in different subzones. Despite this situation, the eight areas showing the most concentrated area of red pixels are all confirmed as exhibiting visible surface water (Table 2). The most apparent water body in zone 2 is the 2.A area (Figure 2.10.2A). This water body covers an area of approximately 80 meters in length and about 20 meters in width. The site is located between significant rocks to the south, dense vegetation to the north and east, and a road to the west. These topographical differences, ether due to rocks or trees, caused inaccuracies in the drainage network definition. This can be seen in inset 2.A, with a perfectly straight flow line from north to south, which does not reflect the actual terrain. Despite those inaccuracies, areas shown as presenting surface water can be seen as well identified (Figure 2.10.2A to 2.10.2D) in zone 2 that is characterized by contrasted vegetation and elevational environments. In zone 2, one area is only situated in the upper section of a drainage line that shows water in a lower section too: area H (Table 2). Overall, the zone 2 results confirm the method allows identification of potential active leakages from the mine tailing even so image texture threshold have been fixed in a different context.

Zone 3 is the last zone surveyed. As for Zone 2, the same image texture threshold value as zone 1 was used. Compared to the 2 previous zones, Zone 3 exhibits the noisiest final raster with numerous isolated red pixels distributed over the visible mosaic (Figure 2.10.3). This situation makes it slightly more difficult to isolate areas with the highest red pixels concentration. The resulting decrease in final raster selectivity illustrates the limits in using the same threshold as fixed using the Zone 1 dataset. Both the differences in orientations, vegetation and topography, and the difference in sunlight angles can potentially explain the degradation of the final raster selectivity. Taken individually, areas of high red pixels concentration are still confirmed as hosting surface water despite their contrasted environments. Zone 3.A (Figure 2.10.3A) is located at the base of the G dike, traversed by a drainage line running along the length of the G dike. Area 3.B (Figure 2.10.3B), located at the base of large rocks outcrops shows narrow streamlet and small water accumulations, with surfaces ranging between 75 cm and 1 m. Area 3.D (Figure 2.10.3D) situates immediately downstream of 3.A, confirming this last area as a potential major water source. Overall, Zone 3 results place into the light 3 areas at the upper section of drainage lines that also show water content in downstream sections. Indeed, areas 3.A, 3.B and 3.C could be considered as potential leaking points from the mine tailing (Table 2).

Table 2.2 Results from the hydrological analysis. For each zone and each area, the water column indicates if the visible orthomosaic confirms the presence of water, the position drainage line column indicates where in the drainage network the targeted area situates, and the connection column indicates any other area situates on the same drainage line. Lines highlighted in blue are the most likely closest to the leakage source

Zone	Area	Water	Position/Drainage line	Connection
Zone 1	A	Confirmed	Lower section	No
	B	Confirmed	Lower section	No
	C	Confirmed	Upper section	Area D
	D	Confirmed	Middle section	Area C
	E	Confirmed	Upper section	No
	F	Confirmed	Upper section	Possibly G
	G	Confirmed	Lower section	Possibly F
	H	Confirmed	Disconnected	No
Zone 2	A	Confirmed	Lower section	Possibly D
	B	Confirmed	Middle section	Areas A and H
	C	Confirmed	Upper section	No
	D	Confirmed	Middle section	Possibly A
	E	Confirmed	Lower section	Area F
	F	Confirmed	Lower section	Area E
	G	Confirmed	Upper section	No
	H	Confirmed	Upper section	Area B
Zone 3	A	Confirmed	Upper section	Area D
	B	Confirmed	Upper section	Area E
	C	Confirmed	Upper section	Area F
	D	Confirmed	Middle section	Area A
	E	Confirmed	Lower section	Area B
	F	Confirmed	Lower section	Area C

2.4.2 Discussion

The use of infrared thermography coupled with image analysis allowed efficiently determining areas of interest for leakages identification. The different sources of information contained in the rasters combined with the image analysis processes made it possible to filter a large amount of data to eliminate negative errors (thermal raster data) and many false positives (image processing rasters), such as those related to vegetation (vNDVI) or slope and shading effects. The multilayer approach with successive raster overlays also adds robustness to the method. The results revealed several critical aspects regarding the distribution of wetlands at the Quémont 2 site. For example, the highest concentrations of water accumulation were observed at the base of dams D, E and F, as well as at the base of dam G, near the former tailings area. These results confirm preliminary field observations and the site's topographic analysis. Additionally, more diffuse zones, concealed by dense vegetation or contained in significant rocky outcrops, were identified. These zones could have been confused with vegetation or slope effects, as they exhibit similar thermal characteristics.

The presence of wetlands along dike G can be explained by the nature of the construction materials used. The use of granular materials without a clay core has greatly impacted on the permeability of dike G, which is likely the cause of water exfiltrations, facilitating hydrological circulation from the new tailings area to the old one. In contrast, dikes D, E, and F are equipped with a clay core, making them less permeable to exfiltration. However, the results also show wetland areas at the foot of these dikes. These areas are more localized, particularly in rocky zones, which are already weakened by multiple fractures, thereby promoting infiltration into the rocks. The methodology applied here also relies on hydrological analysis through drainage lines simulated in ArcGIS Pro®, offering a dynamic aspect to the analysis of the site's hydrological behavior. This dynamic, provided by the drainage network coupled with the final raster, is crucial in attempting to establish a hydrological profile of the site by assigning a flow direction to the detected seepages and attempting to determine their origin. Using this drainage network and information already collected via the previous rasters, such as topography and slopes, it was possible to trace the drainage lines converging towards specific points of interest and deduce the source by tracking the flow lines upstream. Some wetland areas appeared outside these drainage lines, providing additional clues about the sources of flow, depending on the proximity or distance of these flow lines from the identified areas. Thus, it becomes possible to differentiate surface runoff from resurgence or seepage zones.

The hydrological analysis in this study does not fully permit the exact delineation of the sources of underground resurgences, an exercise that must be the subject of further research. In spite of the interpretive constraints in the utilization of the drainage system as one hydrological tool, this approach furnishes significant contextual data for the tailings pond's environmental management. Assignment of flow directions and identification of critical zones allow for an improved and more efficient way to design human interventions by narrowing down the study area to limited zones. Despite the demonstrated potential of the method used in highlighting areas of interest and its robustness to a multitude of variables is evident, it still has important limitations. The filtering of information constituting the final raster remains improvable, as residual anomalies can still infiltrate the intermediate rasters (DTM, shading, topography, or vegetation) and introduce false positives. The precision of thermal sensors is also a potential source of uncertainty in detecting small wetland areas or very small seepage sources. Furthermore, hydrological analysis via drainage line interpretation does not allow for a clear conclusion on the origin of areas identified outside the drainage network or distinguish between resurgence sources and potential leaks. Finally, like all field methods, it is highly dependent on weather conditions and environmental factors. Results accuracy differ between flights due to many factors like time of flight, wind patterns, temperature contrasts, illumination exposure, or any other variable that may affect thermal amplitude, light contrast, or image quality. To minimize these limitations, it may be helpful to integrate other tools or procedures in combination with those employed for data collection, image analysis, or hydrological evaluation. Low-altitude flights would also reduce the resolution limitations of thermal sensors and therefore reduce uncertainty. The image processing stage could be complemented by image analysis supported by deep learning models, which would be trained on datasets where field-verified areas of interest are already identified. These machine learning algorithms would also have the capacity to optimize threshold values based on environmental and meteorological factors, improve the accuracy of image processing, remove false positives, and improve precision.

Finally, hydrological analysis helps to contextualize the results and provide critical insights into underlying hydrological processes. For this reason, it would be relevant to combine the drainage network as a first step in the analysis with other hydrological and geophysical analysis techniques to establish a complete hydrological profile, from surface flows to underground infiltration. Whether for data acquisition or hydrological analysis, monitoring the data over several periods of the year would also help establish baseline observations, essential for identifying anomalies such as leaks based on different pressures exerted on the system, and track the evolution of identified areas to gain further insight into their origin and provenance.

2.5 Conclusion

The methodological approach proposed in this study is based on the use of both efficient and accessible technologies and processes for hydrological detection and analysis, facilitating its application to numerous monitoring and surveillance tasks across a wide range of fields, including research, industry, agriculture or environmental management. A large amount of information was extracted from the drone’s thermal and visible imagery. The image-based rasters, combined with image processing and analysis, enabled the detection and identification of areas of interest marked by the presence of water, such as seepages, resurgences, runoff, or wetland areas. The superposition of the resulting rasters allowed for a precise identification of areas near dikes D, E, F, and G, which show a high concentration of water accumulation zones. The introduction of flow lines, simulated using the hydrological tools of ArcGIS Pro®, made it possible to visualize the hydrological dynamics of the system. By combining the post-processed image analysis data with the drainage network, it was possible to interpret these areas of interest, provide insights into their origins, and attempt to distinguish between simple runoff and resurgence zones. Despite the limitations of the method, particularly regarding the resolution of thermal sensors, uncertainties introduced by image processing, and the inability to precisely determine the origin of the leaks or resurgences, this approach provides a solid foundation for environmental and hydrological monitoring. It also offers the advantage of being adaptable to a wide range of applications while being cost-effective and easy to implement. The results confirm the effectiveness of this methodology while also opening up opportunities for future improvements, such as the integration of complementary tools like geophysical techniques and image processing assisted by machine learning models.

CONCLUSION

L’étude menée sur le site minier Quémont 2 a mené à l’obtention de résultats assez concluants et a permis de démontrer que l’approche multiméthode d’imagerie thermique infrarouge (IR) superposée à d’autres indices, tels que le vNDVI, les pentes et l’ombrage, a permis d’isoler efficacement les zones humides et de remonter les sources potentielles d’exfiltrations. En superposant ces indices avec un réseau de drainage, il a été possible de différencier les ruissellements de surface des écoulements souterrains. L’atout majeur de cette méthode réside dans sa capacité à réduire significativement les faux positifs en combinant plusieurs types de données et d’indice, en appliquant un seuillage optimisé par des algorithmes d’apprentissage automatique. Cette approche vise à améliorer la précision des détections par rapport aux méthodes conventionnelles basées uniquement sur l’analyse thermique, contenant bien souvent une quantité importante de bruits résiduels ou de faux positifs. De plus, l’utilisation d’un drone équipé d’une double caméra (visible et thermique) a facilité une acquisition rapide et à haute résolution des données, tout en renforçant la faisabilité opérationnelle pour de la surveillance environnementale.

Cependant, certaines limites subsistent et nécessitent des améliorations pour renforcer et optimiser la robustesse de la méthode. Dans un premier temps, la résolution du capteur thermique utilisé constitue la principale contrainte et impacte fortement la précision des détections, en particulier dans les environnements complexes où les contrastes thermiques sont faibles. L’utilisation de caméras thermiques à plus haute résolution et avec une meilleure sensibilité dans le spectre IR pourrait affiner la détection des suintements diffus ou fins. D’autre part, les conditions météorologiques jouent un rôle crucial dans l’acquisition des images thermiques en influençant la qualité des contrastes de température. L’intégration d’un modèle de correction prenant en compte les variations diurnes de température et les conditions atmosphériques permettrait d’améliorer la fiabilité des résultats. En normalisant les écarts thermiques liés au moment de l’acquisition des images, et en calibrant les données thermiques avec des références environnementales mesurées sur le terrain à différents moments, il serait possible d’ajuster les seuils de détection pour minimiser l’impact des conditions extérieures sur l'interprétation des images. En complément, une amélioration des protocoles d'acquisition des données, notamment en optimisant les heures et jours de vol de drone pour maximiser le contraste thermique pourrait renforcer l'efficacité des mesures.

Par ailleurs, l'utilisation de l'intelligence artificielle pour affiner l'interprétation des images ouvre des perspectives intéressantes. L'application de réseaux de neurones convolutionnels (CNN) permettrait d'automatiser et d'optimiser davantage le processus de filtrage des faux positifs et d'accroître la précision de classification des anomalies détectées. Il est important de préciser que cette méthode à elle seule ne vise pas à remplacer les techniques géophysiques usuelles mais constitue un complément non négligeable. De ce fait, l'association avec des techniques géophysiques, telles que la tomographie de résistivité électrique (ERT) ou le radar à pénétration de sol (GPR), pourrait offrir une approche multi-capteurs permettant une validation croisée des zones d'exfiltration identifiées.

Enfin, cette méthodologie pourrait être élargie à d'autres secteurs d'activité et à d'autres sites présentant des problématiques similaires, notamment dans le cadre de la surveillance des barrages, des digues de protection ou encore des infrastructures hydrauliques en milieu urbain. Son adaptabilité, son accessibilité et sa capacité à fournir des résultats exploitables rapidement en font une alternative prometteuse aux méthodes traditionnelles de suivi environnemental souvent coûteuses et difficiles à mettre en place. Ainsi, bien que des améliorations techniques soient encore nécessaires, cette approche intégrée représente une avancée intéressante pour la détection et la gestion des fuites dans les environnements miniers, contribuant ainsi à une meilleure préservation des ressources hydriques et à la réduction des impacts environnementaux.

LISTE DE RÉFÉRENCES BIBLIOGRAPHIQUES

Adetokunbo, P., A. Ismail, F. Mewafy and O. Sanuade (2024). Geophysical Characterization and Seepage Detection of the Chimney Rock Dam Embankment Near Salina, Oklahoma. *Water (Switzerland)* 16(9). https://doi.org/10.3390/w16091224

Ampatzidis, Y., Partel, V., & Costa, L. (2020). Agroview: Cloud-based application to process, analyze and visualize UAV-collected data for precision agriculture applications utilizing artificial intelligence. *Computers and Electronics in Agriculture*, 174, 105457. https://doi.org/10.1016/j.compag.2020.105457

Anderson, M. C., Norman, J. M., Kustas, W. P., Houborg, R., Starks, P. J., & Agam, N., 2008. A thermal-based remote sensing technique for routine mapping of land-surface carbon, water and energy fluxes from field to regional scales. *Remote Sensing of Environment*, 112(12), 4227-4241. https://doi.org/10.1016/j.rse.2008.07.009

Baker, E. A., Lautz, L. K., McKenzie, J. M., & Aubry-Wake, C., 2019. Improving the accuracy of time-lapse thermal infrared imaging for hydrologic applications. *Journal of hydrology*, 571, 60-70. https://doi.org/10.1016/j.jhydrol.2019.01.053

Baluja, J., Diago, M. P., Balda, P., Zorer, R., Meggio, F., Morales, F., & Tardaguila, J., 2012. Assessment of vineyard water status variability by thermal and multispectral imagery using an unmanned aerial vehicle (UAV). *Irrigation science*, 30, 511-522. https://doi.org/10.1007/s00271-012-0382-9

Barbieri, A. L., De Arruda, G. F., Rodrigues, F. A., Bruno, O. M., & da Fontoura Costa, L. (2011). An entropy-based approach to automatic image segmentation of satellite images. *Physica A: Statistical Mechanics and its Applications*, 390(3), 512-518. https://doi.org/10.1016/j.physa.2010.10.015

Ben Abdelghani, F., M. Aubertin, R. Simon and R. Therrien (2015). Numerical simulations of water flow and contaminants transport near mining wastes disposed in a fractured rock mass. *International Journal of Mining Science and Technology* 25(1): 37-45. https://doi.org/10.1016/j.ijmst.2014.11.003

Bharati, M. H., Liu, J. J., & MacGregor, J. F., 2004. Image texture analysis: methods and comparisons. *Chemometrics and intelligent laboratory systems*, 72(1), 57-71. https://doi.org/10.1016/j.chemolab.2004.02.005

Blaschke, T., Lang, S., Lorup, E., Strobl, J., & Zeil, P., 2000. Object-oriented image processing in an integrated GIS/remote sensing environment and perspectives for environmental applications. *Environmental information for planning, politics and the public*, 2(1995), 555-570.

Chaudhary, A. S., & Chaturvedi, D. K., 2017. Observing hotspots and power loss in solar photovoltaic array under shading effects using thermal imaging camera. *Int. J. Electr. Mach. Drives*, 3(1), 15-23.

Chen, G., Y. Ye, N. Yao, N. Hu, J. Zhang and Y. Huang (2021). A critical review of prevention, treatment, reuse, and resource recovery from acid mine drainage. *Journal of Cleaner Production* 329. https://doi.org/10.1016/j.jclepro.2021.129666

Costa, L., Nunes, L., & Ampatzidis, Y., 2020. A new visible band index (vNDVI) for estimating NDVI values on RGB images utilizing genetic algorithms. *Computers and Electronics in Agriculture*, 172, 105334. https://doi.org/10.1016/j.compag.2020.105334

Deitchman, R. S. and S. P. Loheide II (2009). Ground-based thermal imaging of groundwater flow processes at the seepage face. *Geophysical Research Letters* 36(14). https://doi.org/10.1029/2009GL038103

El Mrabet, E., 2021. Développement d'approches géophysiques, d'imagerie thermique et de modélisation pour l'évaluation des processus hydrologiques au sein d'un parc à résidus miniers. *Polytechnique de Montréal, Université de Montréal & Université du Québec.*

Esri Inc. (2023). ArcGIS Pro (Version 3.1.3) [Logiciel]. Repéré à https://www.esri.ca/

Feng, Y., Wang, J., Bai, Z., & Reading, L. (2019). Effects of surface coal mining and land reclamation on soil properties: A review. *Earth-Science Reviews*, 191, 12-25. https://doi.org/10.1016/j.earscirev.2019.02.015

Frodella, W., Gigli, G., Morelli, S., Lombardi, L., & Casagli, N., 2017. Landslide mapping and characterization through infrared thermography (IRT): Suggestions for a methodological approach from some case studies. *Remote Sensing*, 9(12), 1281. https://doi.org/10.3390/rs9121281

Gareev A, Gareev E (2023) Characteristics of environmental degradation in mining areas (A case study of the Southern Trans-Urals). *Ann Environ Sci Toxicol* 7(1): 004-012. https://doi.org/10.17352/aest.000064

Garrido, I., S. Lagüela, R. Otero and P. Arias (2020). Thermographic methodologies used in infrastructure inspection: A review—Post-processing procedures. *Applied Energy* 266: 114857. https://doi.org/10.1016/j.apenergy.2020.114857

Ghomshei, M. M. and D. M. Allen (2000). Hydrochemical and stable isotope assessment of tailings pond leakage, Nickel Plate Mine, British Columbia. *Environmental Geology* 39(8): 937-944.

Gomez Llerena, J. A., M. Ghahramanieisalou and J. Sattarvand (2023). Tackling Geotechnical Risks in Tailings Dams Using High-Resolution UAV Imaging and Advanced Image Processing. *Geotechnical Special Publication*. https://doi.org/10.1061/9780784484975.024

Gustaytis, M. A., Myagkaya, I. N., & Chumbaev, A. S. (2018). Hg in snow cover and snowmelt waters in high-sulfide tailing regions (Ursk tailing dump site, Kemerovo region, Russia). *Chemosphere*, 202, 446-459. https://doi.org/10.1016/j.chemosphere.2018.03.076

Hou, Y., Zhao, Y., Lu, J., Wei, Q., Zang, L., & Zhao, X. (2023). Environmental contamination and health risk assessment of potentially toxic trace metal elements in soils near gold mines–a global meta-analysis. *Environmental Pollution*, 330, 121803. https://doi.org/10.1016/j.envpol.2023.121803

Hung, C. C., Song, E., & Lan, Y. (2019). Image texture analysis (pp. 201-232). Cham: *Springer International Publishing*.

Janga, B., Asamani, G. P., Sun, Z., & Cristea, N. (2023). A review of practical ai for remote sensing in earth sciences. *Remote Sensing*, 15(16), 4112. https://doi.org/10.3390/rs15164112

Jian, J., J. Lu, Q. Guo, J. Wang, L. Sun, D. Mao and Y. Wang (2024). Characterization and Quantification of Dam Seepage Based on Resistivity and Geological Information. *Water (Switzerland)* 16(17). https://doi.org/10.3390/w16172410

Jonnalagadda, S. B. and P. V. V. P. Rao (1993). Toxicity, bioavailability and metal speciation. *Comparative Biochemistry and Physiology Part C: Pharmacology, Toxicology and Endocrinology* 106(3): 585-595. https://doi.org/10.1016/0742-8413(93)90215-7

Karaca, O., Cameselle, C., & Reddy, K. R. (2018). Mine tailing disposal sites: contamination problems, remedial options and phytocaps for sustainable remediation. *Reviews in Environmental Science and Bio/Technology*, 17, 205-228. https://doi.org/10.1007/s11157-017-9453-y

Khonina, S. N., Kazanskiy, N. L., Efimov, A. R., Nikonorov, A. V., Oseledets, I. V., Skidanov, R. V., & Butt, M. A. (2024). A perspective on the artificial intelligence's transformative role in advancing diffractive optics. *iscience*, 27(7). https://doi.org/10.1016/j.isci.2024.110270

Kossoff, D., W. E. Dubbin, M. Alfredsson, S. J. Edwards, M. G. Macklin and K. A. Hudson-Edwards (2014). Mine tailings dams: Characteristics, failure, environmental impacts, and remediation. *Applied Geochemistry* 51: 229-245. https://doi.org/10.1016/j.apgeochem.2014.09.010

Lachhab, A., E. M. Benyassine, M. Rouai, A. Dekayir, J. C. Parisot and M. Boujamaoui (2020). Integration of Multi geophysical Approaches to Identify Potential Pathways of Heavy Metals Contamination - A Case Study in Zeida, Morocco. *Journal of Environmental and Engineering Geophysics* 25(3): 415-423. https://doi.org/10.32389/JEEG9-067

Lega, M., & Napoli, R. M. (2010). Aerial infrared thermography in the surface waters contamination monitoring. *Desalination and water treatment*, 23(1-3), 141-151. https://doi.org/10.5004/dwt.2010.1988

Li, P., L. Tang, S. Zhang, P. Ming, Y. Wang, Q. Zhan and J. Wen (2024). Leakage identification and numerical simulation of embankment dams based on infrared thermal imaging. *Structural Health Monitoring*. https://doi.org/10.1177/14759217241287868

Llerena, J. A. G. and J. Sattarvand (2023). DRONE-BASED APPLICATIONS FOR TAILINGS DAM MONITORING. SME *Annual Conference and Expo 2023*.

Luquet, D., Bégué, A., Vidal, A., Clouvel, P., Dauzat, J., Olioso, A., ... & Tao, Y., 2003. Using multidirectional thermography to characterize water status of cotton. *Remote Sensing of Environment*, 84(3), 411-421. https://doi.org/10.1016/S0034-4257(02)00131-1

Manfreda, S., McCabe, M. F., Miller, P. E., Lucas, R., Pajuelo Madrigal, V., Mallinis, G., ... & Toth, B. (2018). On the use of unmanned aerial systems for environmental monitoring. *Remote sensing*, 10(4), 641. https://doi.org/10.3390/rs10040641

Mhiri, O., 2023. Analyse de la dynamique hydrologique/hydrogéologique d'un résidu minier. *École de Technologie Supérieure, Université du Québec*.

Moreira, C. A., L. Guireli Netto, P. L. Camarero, F. B. Bertuluci, M. E. Hartwig and R. Domingos (2022). Application of electrical resistivity tomography (ERT) in uranium mining earth dam. *Journal of Geophysics and Engineering* 19(6): 1265-1279. https://doi.org/10.1093/jge/gxac082

Morgan, S., Collins, J., 2022. Use of thermal infrared (TIR) imagery to identify potential groundwater discharge areas associated with contaminants of potential concern. *Proceedings of the RemTech 2022 conference*, Banff, AB, Canada.

Mundy, E., Gleeson, T., Roberts, M., Baraer, M., & McKenzie, J. M., 2017. Thermal imagery of groundwater seeps: Possibilities and limitations. *Groundwater*, 55(2), 160-170. https://doi.org/10.1111/gwat.12451

Navarro-Ciurana, D., A. Saleta-Daví, N. Otero, C. Torrentó, C. Quintana-Sotomayor, D. S. Miguel-Cornejo, M. Musalem-Jara, G. Novoa-Godoy, C. Carrasco-Jaramillo, E. Aguirre-Dueñas, M. A. Escudero-Vargas and A. Soler (2023). Quantifying the potential seepage from porphyry copper tailing impoundments using a multi-isotopic approach. *Science of The Total Environment* 890: 164446. https://doi.org/10.1016/j.scitotenv.2023.164446

OpenDroneMap (2022). WebODM (Version 1.9.16) [Logiciel]. Repéré à https://opendronemap.org/

Otsu, N. (1975). A threshold selection method from gray-level histograms. *Automatica*, 11(285-296), 23-27.

Ozotta, O., & Gerla, P. J., 2021. Mapping Groundwater Seepage in a Fen Using Thermal Imaging. *Geosciences*, 11(1), 29. https://doi.org/10.3390/geosciences11010029

Pandey, P., Gleeson, T., & Baraer, M. (2013). Toward quantifying discrete groundwater discharge from frozen seepage faces using thermal infrared images. *Geophysical research letters*, 40(1), 123-127. https://doi.org/10.1029/2012GL054315

Pazzi, V., S. Morelli and R. Fanti (2019). A Review of the Advantages and Limitations of Geophysical Investigations in Landslide Studies. *International Journal of Geophysics* 2019. https://doi.org/10.1155/2019/2983087

Pix4D SA (2022). Pix4Dmapper (Version 4.8.1) [Logiciel].
Repéré à https://www.pix4d.com/

Poisson, J., M. Chouteau, M. Aubertin and D. Campos (2009). Geophysical experiments to image the shallow internal structure and the moisture distribution of a mine waste rock pile. *Journal of Applied Geophysics* 67(2): 179-192. https://doi.org/10.1016/j.jappgeo.2008.10.011

Punia, A. Role of temperature, wind, and precipitation in heavy metal contamination at copper mines: a review. *Environ Sci Pollut Res* 28, 4056–4072 (2021). https://doi.org/10.1007/s11356-020-11580-8

Ramani, R. V. (2012). Surface mining technology: progress and prospects. *Procedia Engineering*, 46, 9-21. https://doi.org/10.1016/j.proeng.2012.09.440

Romero, A., González, I., Martín, J. M., Vázquez, M. A., & Ortiz, P. (2015). Risk assessment of particle dispersion and trace element contamination from mine-waste dumps. *Environmental geochemistry and health*, 37, 273-286.
https://doi.org/10.1007/s10653-014-9645-0

Rösner, T., & Van Schalkwyk, A. (2000). The environmental impact of gold mine tailings footprints in the Johannesburg region, South Africa. *Bulletin of Engineering Geology and the Environment*, 59, 137-148. https://doi.org/10.1007/s100640000037

Schrott, L. and O. Sass (2008). Application of field geophysics in geomorphology: Advances and limitations exemplified by case studies. *Geomorphology* 93(1-2): 55-73. https://doi.org/10.1016/j.geomorph.2006.12.024

Shrestha, R. K., & Lal, R. (2011). Changes in physical and chemical properties of soil after surface mining and reclamation. *Geoderma*, 161(3-4), 168-176. https://doi.org/10.1016/j.geoderma.2010.12.015

Song, W.; Song, W.; Gu, H.; Li, F., 2020. Progress in the Remote Sensing Monitoring of the Ecological Environment in Mining Areas. *Int. J. Environ. Res. Public Health*, 17(6):1846. https://doi.org/10.3390/ijerph17061846

Šourková, M., Frouz, J., & Šantrùčková, H. (2005). Accumulation of carbon, nitrogen and phosphorus during soil formation on alder spoil heaps after brown-coal mining, near Sokolov (Czech Republic). *Geoderma*, 124(1-2), 203-214. https://doi.org/10.1016/j.geoderma.2004.05.001

Still, C., Powell, R., Aubrecht, D., Kim, Y., Helliker, B., Roberts, D., ... & Goulden, M., 2019. Thermal imaging in plant and ecosystem ecology: applications and challenges. *Ecosphere*, 10(6), e02768. https://doi.org/10.1002/ecs2.2768

The MathWorks, Inc. (2022). MATLAB and Image Processing Toolbox (Version R2022b) [Logiciel]. Repéré à https://www.mathworks.com/

Thomson, S., Brooks, T., Huang, Y., Weick, J., Fisher, D. K., DeFauw, S., ... & English, P. (2015). Thermal imaging: from irrigation management to finding leaks at the levee. *Resource Magazine*, 22(3), 10-13.

Wang, X., J. Liang and L. Rongliang (2024). In-site experimental study on the effects of infrared thermal imaging technology on levee leakage detection. *Scientific Reports* 14(1): 26032. https://doi.org/10.1038/s41598-024-77383-w

Wang, Z. F., Yu, Y. F., Wang, J., Zhang, J. Q., Zhu, H. L., Li, P., ... & Chen, J. P. (2022). Convolutional neural-network based automatic dam-surface seepage defect identification from thermograms collected from UAV-mounted thermal imaging camera. *Construction and Building Materials*, 323, 126416. https://doi.org/10.1016/j.conbuildmat.2022.126416

Whitehead, K., Hugenholtz, C., 2014. Remote sensing of the environment with small unmanned aircraft systems (UASs), part 1: review of progress and challenges. *Journal of Unmanned Vehicle Systems*. 02(03): 69:85. https://doi.org/10.1139/juvs-2014-0006

Wong, H. K. T., Gauthier, A., & Nriagu, J. O. (1999). Dispersion and toxicity of metals from abandoned gold mine tailings at Goldenville, Nova Scotia, Canada. *Science of the Total Environment*, 228(1), 35-47. https://doi.org/10.1016/S0048-9697(99)00021-2

Xu, X., Xu, S., Jin, L., & Song, E., 2011. Characteristic analysis of Otsu threshold and its applications. *Pattern recognition letters*, 32(7), 956-961. https://doi.org/10.1016/j.patrec.2011.01.021

Yang, J., Wang, W., Lin, G., Li, Q., Sun, Y., & Sun, Y., 2019. Infrared thermal imaging-based crack detection using deep learning. *Ieee Access*, 7, 182060-182077. https://doi.org/10.1109/ACCESS.2019.2958264

Yasuda, N., N. R. Thomson and J. F. Barker (2010). Performance evaluation of a tailings pond seepage collection system. *Canadian Geotechnical Journal* 47(12): 1305-1315. https://doi.org/10.1139/T10-029

Zhang, B., Wu, D., Zhang, L., Jiao, Q., & Li, Q., 2012. Application of hyperspectral remote sensing for environment monitoring in mining areas. *Environmental Earth Sciences*, 65, 649-658. https://doi.org/10.1007/s12665-011-1112-y